Systems-guided forward genetic screen reveals a critical role of the replication stress response protein ETAA1 in T cell clonal expansion

Lisa A. Miosge[a], Yovina Sontani[a], Aaron Chuah[a], Keisuke Horikawa[a], Tiffany A. Russell[a,1], Yan Mei[a], Mayura V. Wagle[a], Debbie R. Howard[a], Anselm Enders[a], David C. Tscharke[a], Christopher C. Goodnow[a,b,c,2,3], and Ian A. Parish[a,2,3]

[a]John Curtin School of Medical Research, Australian National University, Canberra, ACT 2601, Australia; [b]Garvan Institute of Medical Research, Sydney, New South Wales 2010, Australia; and [c]St. Vincent's Clinical School, University of New South Wales, Darlinghurst, New South Wales 2010, Australia

Contributed by Christopher C. Goodnow, May 18, 2017 (sent for review April 7, 2017; reviewed by Rafi Ahmed and Bruce Stillman)

T-cell immunity requires extremely rapid clonal proliferation of rare, antigen-specific T lymphocytes to form effector cells. Here we identify a critical role for ETAA1 in this process by surveying random germ line mutations in mice using exome sequencing and bioinformatic annotation to prioritize mutations in genes of unknown function with potential effects on the immune system, followed by breeding to homozygosity and testing for immune system phenotypes. Effector $CD8^+$ and $CD4^+$ T-cell formation following immunization, lymphocytic choriomeningitis virus (LCMV) infection, or herpes simplex virus 1 (HSV1) infection was profoundly decreased despite normal immune cell development in adult mice homozygous for two different *Etaa1* mutations: an exon 2 skipping allele that deletes Gly78-Leu119, and a Cys166Stop truncating allele that eliminates most of the 877-aa protein. ETAA1 deficiency decreased clonal expansion cell autonomously within the responding T cells, causing no decrease in their division rate but increasing TP53-induced mRNAs and phosphorylation of H2AX, a marker of DNA replication stress induced by the ATM and ATR kinases. Homozygous ETAA1-deficient adult mice were otherwise normal, healthy, and fertile, although slightly smaller, and homozygotes were born at lower frequency than expected, consistent with partial lethality after embryonic day 12. Taken together with recently reported evidence in human cancer cell lines that ETAA1 activates ATR kinase through an exon 2-encoded domain, these findings reveal a surprisingly specific requirement for this ATR activator in adult mice restricted to rapidly dividing effector T cells. This specific requirement may provide new ways to suppress pathological T-cell responses in transplantation or autoimmunity.

T cell | DNA damage | replication stress | Etaa1 | immunity

T lymphocytes play an essential role in adaptive immunity against pathogenic microbes and tumors. In the absence of stimulation, peripheral T cells remain in a quiescent naïve state. When a microbial antigen binds to the T-cell receptor on a rare antigen-specific T-cell, the cell undergoes rapid proliferation, clonal expansion, and effector differentiation (1, 2). Failure of antigen-specific T cells to proliferate in response to replicating virus, bacterium, or yeast can lead to uncontrolled fatal infection. For this reason, T-cell proliferation in vivo in response to infection is one of fastest cell proliferation rates known (3). Fast cell division undoubtedly places enormous stress on proliferating T cells. T cells cope with the metabolic demands of rapid growth by undergoing a dramatic metabolic shift to a more anabolic metabolic state (4); however, how T cells cope with all of the challenges of rapid DNA replication is unclear. The stress associated with DNA replication in proliferating T cells is illustrated by their heightened susceptibility to the DNA topoisomerase II inhibitor etoposide (5, 6). Identifying critical components for T-cell replication in vivo would provide new targets for developing immunosuppressive drugs to prevent damaging T-cell responses in organ transplantation and autoimmune disease.

Rapid genome replication presents unique challenges to proliferating cells (7). During DNA replication, the replication machinery often encounters "roadblocks" in the form of spontaneous DNA damage, collisions with the transcription machinery, or insufficient deoxynucleotide substrates for DNA polymerase (8). Such disruptions can interfere with DNA replication and cause stalling or collapse of the replication fork. Replication stalling or collapse leads to the exposure of single-stranded DNA (ssDNA) by the continued activity of DNA helicase, and this ssDNA will be attacked by nucleases to create double-stranded (ds) breaks in the absence of an appropriate cellular response. Thus, cells have evolved a replication stress response that first detects stalled replication forks and then acts to insulate the ssDNA against damage and to arrest cell cycle progression. The Replication Protein A (RPA) complex binds and protects ssDNA at stalled replication forks, and recruits a complex set of repair and restart proteins that includes the protein kinase Ataxia Telangiectasia and Rad3-Related (ATR). ATR elicits checkpoint signaling by phosphorylating BRCA1, CHEK1, MCM2, TP53, and other proteins that inhibit DNA replication and promote DNA repair, recombination, and apoptosis, and also phosphorylates Ser-139 of histone H2AX (denoted γH2AX), which serves as an experimental

Significance

T cells are required for control of many intracellular infections, and a critical component of T cell immunity is the proliferative expansion of effector T cells upon stimulation. Using a forward-based genetic screen, we identify the mouse *Etaa1* gene as critically important for T cell proliferative expansion after vaccination and during infection. Consistent with recent findings that ETAA1 prevents DNA damage during proliferation, our data demonstrate elevated DNA damage within *Etaa1*-deficient effector T cells, which likely leads to cell death. This phenotype is restricted to effector T cell proliferation, with T cell development and other immune parameters remaining normal. Thus, ETAA1 may represent a novel drug target to selectively suppress pathological T cell responses in transplantation or autoimmunity.

Author contributions: L.A.M., K.H., A.E., D.C.T., C.C.G., and I.A.P. designed research; L.A.M., Y.S., A.C., K.H., T.A.R., Y.M., M.V.W., D.R.H., and I.A.P. performed research; K.H. contributed new reagents/analytic tools; L.A.M., Y.S., A.C., K.H., T.A.R., Y.M., M.V.W., D.R.H., D.C.T., C.C.G., and I.A.P. analyzed data; and L.A.M., C.C.G., and I.A.P. wrote the paper.

Reviewers: R.A., Emory University; and B.S., Cold Spring Harbor Laboratory.

The authors declare no conflict of interest.

Data deposition: RNA-seq data have been deposited in the Gene Expression Omnibus (GEO) database, https://www.ncbi.nlm.nih.gov/geo (accession no. GSE99144).

[1]Present address: Department of Microbial Sciences, University of Surrey, Guildford, United Kingdom.

[2]C.C.G. and I.A.P. contributed equally to this work.

[3]To whom correspondence may be addressed. E-mail: c.goodnow@garvan.org.au or ian.parish@anu.edu.au.

This article contains supporting information online at www.pnas.org/lookup/suppl/doi:10.1073/pnas.1705795114/-/DCSupplemental.

marker of DNA replication stress and damage. ATR phosphorylation of CHEK1 and MCM2 is stimulated by Topoisomerase II-Binding Protein 1 (TOPBP1). A universal requirement in rapidly dividing cells for the core components of the replication stress response is implied by early embryonic lethality in mice homozygous for knockout or hypomorphic mutations in *Rpa1*, *Atr*, and *Topbp1* (9–13); however, whether specific components are selectively needed to insulate proliferating effector T cells against replication stress is unclear.

At the time that we conducted the studies described herein, the *Ewing's tumor- associated antigen 1* (*Etaa1*) gene had no known function, encoding a pioneer protein with no recognizable domains that had been isolated by an antibody against a surface antigen on Ewing's tumors (14). Because *Etaa1* mRNA was most abundant in T and B lymphocytes among all mouse tissues except embryonic stem cells (BioGPS data for probe 1453064_at; biogps.org) (15) and encoded part of the "dark proteome," it was a good candidate to test for immune system phenotypes in a systems-guided forward genetics screen. The screen starts by exome sequence analysis to identify large numbers of heterozygous de novo point mutations in the mouse genome induced at random in first-generation (G1) offspring of inbred C57BL/6 mice treated with ethylnitrosourea (ENU) (16, 17). Computational filtering then identifies mutations that are predicted to be damaging in genes of unknown function, focusing on genes with indirect systems-level evidence of a role in the immune system. The mutation of interest is then brought to homozygosity by intercrossing heterozygous G2 carriers and then genotyping the G3 offspring to identify the 25% expected to be homozygous for the mutation of interest. These homozygotes and all their G3 siblings are tested for a battery of immune phenotypes, and the data are analyzed to detect phenotypic changes that segregate with the mutation of interest.

Here we describe the use of a systems-guided forward genetics screen to reveal that homozygous *Etaa1* loss-of-function mutations permitted normal mouse development, albeit with >50% embryonic loss, had no discernable effect on T and B lymphocyte development or T-cell proliferation in vitro but caused a profound, cell-intrinsic decrease in T-cell proliferation in vivo in response to immunization or viral infection. Early in the response to virus infection, the rapidly dividing mutant T cells display a strong induction of p53-induced DNA damage response gene sets and increased γH2AX. These results, together with four recent studies demonstrating that ETAA1 associates with RPA at stalled DNA replication forks to stimulate ATR and the replication stress response in nonlymphoid cancer cells in tissue culture (18–21), reveal a highly specific role for ETAA1 in adult mice regulating replication stress during the formation of effector T cells after infection or immunization.

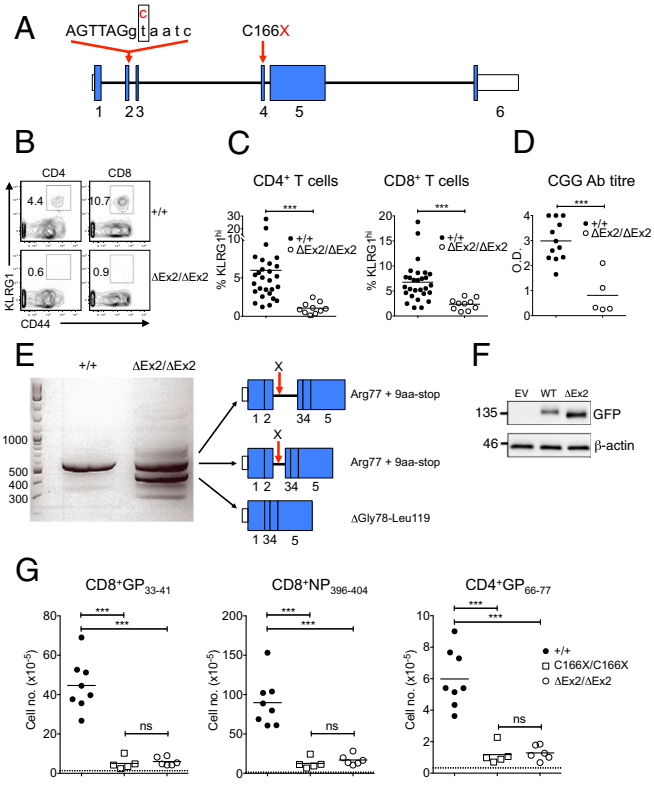

Fig. 1. *Etaa1* is required for effector T-cell expansion after immunization and LCMV infection. (*A*) Schematic of the *Etaa1* gene, with exons numbered, coding sequence in blue, and location of the *ΔEx2* splice and C166X mutations. (*B–D*) Representative and compiled data showing KLRG1^{hi} effector T-cell percentage (*B* and *C*) and CGG antibody titer (*D*) in blood at day 14 after immunization of *Etaa1*$^{+/+}$ or *Etaa1*$^{\Delta Ex2/\Delta Ex2}$ mice with CGG and inactivated *B. pertussis*. (*E*) Agarose gel electrophoresis of PCR-amplified cDNA using primers in *Etaa1* exons 1 and 5 from *Etaa1*$^{+/+}$ or *Etaa1*$^{\Delta Ex2/\Delta Ex2}$ spleen cells. The mRNA structure of the indicated bands deduced by Sanger sequencing is shown on the right. (*F*) Wild-type or *ΔEx2* mutant *Etaa1* cDNA sequences fused to GFP were transiently transfected into HEK293T cells. Western blot analysis was conducted on total cell lysates prepared at 48 h after transfection to assess GFP-fused ETAA1 or control β-actin protein expression. (*G*) *Etaa1*$^{+/+}$, *Etaa1*$^{C166X/C166X}$, or *Etaa1*$^{\Delta Ex2/\Delta Ex2}$ mice were infected with LCMV-Arm, and the numbers of splenic CD8$^+$GP$_{33-41}$, CD8$^+$NP$_{396-404}$, and CD4$^+$GP$_{66-77}$ tetramer-positive cells were assessed at day 8 postinfection. The dotted line in each graph indicates the limit of detection based on staining of uninfected animals. ***$P < 0.001$, *t* test (*C* and *D*) or one-way ANOVA (*G*).

Results

Etaa1 Mutant Mice Have Defective Effector T-Cell Responses After Vaccination. A systems-guided forward genetics screen was conducted on de novo heterozygous point mutations revealed by exome sequencing of hundreds of G1 offspring of ENU-treated C57BL/6 male mice (16, 17). G1 mouse IGL1100 had an *Etaa1* point mutation in the intron between exons 2 and 3, predicted to be damaging because it substituted a C nucleotide for the essential +2 T of the splice donor consensus sequence (Fig. 1*A*). After outcrossing the G1 mouse with unrelated G1 mice to segregate other unlinked heterozygous mutations, the G2 offspring were genotyped to identify and intercross the 50% of animals heterozygous for the *Etaa1* mutation. The G3 offspring resulting from the intercrosses were genotyped for the *Etaa1* mutation to identify homozygous, heterozygous, and wild-type siblings, which were then screened for immune phenotypes.

Flow cytometry screening of blood samples from the G3 offspring revealed normal frequencies of lymphocytes and subsets of B cells and CD4$^+$ and CD8$^+$ T cells in the *Etaa1* mutant homozygotes (see below). However, after challenge with an immunization mixture of inactivated *Bordetella pertussis* and chicken gamma globulin (CGG), the homozygous mutants failed to generate the population of effector KLRG1^{hi} CD4$^+$ and CD8$^+$ T cells normally seen at day 14 postimmunization in the blood of wild-type mice (Fig. 1 *B* and *C*). In further generations of outcrossing to C57BL/6 mice and intercrossing *Etaa1* heterozygotes, the lack of effector T cells after immunization correlated completely with homozygosity for the *Etaa1* mutation, whereas this trait segregated from all other linked and unlinked mutations present in the original G1 IGL1100 founder mouse. The *Etaa1* homozygous mutants also had lower titers of T-cell–dependent antibody at 14 d after immunization (Fig. 1*D*), although this phenotype often reached comparable titers to those seen in wild-type mice by 28 d.

Based on the striking effector T-cell deficit after immunization, the molecular effect of the *Etaa1* Exon 2 splice donor mutation was determined by preparing spleen cDNA from homozygous mutant and wild-type littermates. PCR amplification of *Etaa1* cDNA with primers in exons 1 and 5 yielded a single product of the expected size from wild-type cDNA, but yielded two major and several minor aberrantly sized products from mutant cDNA (Fig. 1*E*). Sequencing of the PCR products

revealed one of the two main PCR products in the mutant mice spliced exon 1 to exon 2 normally, but skipped the normal exon 2 splice donor, instead splicing to exon 3 from a cryptic splice donor at +25 nucleotides in intron 2. The retained intronic 25 nucleotides encoded nine amino acids before an in-frame stop codon, resulting in a truncated product containing only the first 77 amino acids of the 877-residue ETAA1 protein. The other major product in the mutant mice was smaller than wild-type because it skipped exon 2, splicing exon 1 to exon 3 to produce an in-frame deletion of 42 amino acids (Gly78-Leu119 inclusive). The third and largest sequenced product retained the entire exon 2/3 intron, which also introduced the in-frame stop codon mentioned above. When the full length wild-type or exon 2-deleted *Etaa1* sequence was expressed as GFP fusion proteins in transiently transfected cells, they produced comparable amounts of protein (Fig. 1*F*) that was localized primarily in the nucleus in both cases. Because one of the main aberrantly spliced products encodes all the ETAA1 protein except the 42 residues encoded by exon 2, we refer to this *Etaa1* mutant allele as *ΔEx2*.

An independent *Etaa1* mutant allele was identified in the exome sequence of another G1 mouse, IGL00465. This allele is a point mutation in exon 4, changing the Cys166 codon sequence from TGT to TGA to create a premature stop codon at amino acid 166 of the 877-aa mouse ETAA1 protein (Fig. 1*A*). Thus, the $Etaa1^{C166X}$ mutation would be predicted to result in a null allele.

To extend the T-cell analysis, mice homozygous for the two different *Etaa1* mutations were bred in parallel and infected with lymphocytic choriomeningitis virus Armstrong (LCMV-Arm) strain, which establishes an acute infection and provokes a robust and well-characterized T-cell response. The LCMV antigen-specific T-cell response was assessed at the peak of the T-cell response at day 8 postinfection. Thus, this test would resolve whether the reduction in effector T cells observed at day 14 postimmunization in the $Etaa1^{\Delta Ex2/\Delta Ex2}$ mutant mice was due to defective initial clonal expansion or excessive contraction after the peak of the response at day 7–8. In addition, because terminally differentiated $KLRG1^{hi}$ effector T cells represent only one subset of effectors (22, 23), testing for LCMV antigen-specific T cells would resolve if the *Etaa1* mutant mice had a selective deficiency in the generation of $KLRG1^{hi}$ effectors or a general defect in clonal expansion of antigen-specific T cells.

Flow cytometry staining with tetramers enabled enumeration of $CD8^+$ T cells specific for two immunodominant epitopes of the virus, $GP_{33–41}$ and $NP_{396–404}$, and $CD4^+$ T cells specific for the immunodominant $GP_{66–77}$ virus epitope. Compared with wild-type controls, there were 10-fold fewer antigen-specific $CD8^+$ and $CD4^+$ T cells in LCMV-infected homozygotes for either the exon 2 deleted or the C166X null allele, although there was still a detectable effector T-cell response in both strains (Fig. 1*G*). A similar decrease in effector cell number was observed when antigen-specific T cells were enumerated by peptide-stimulated IFN-γ expression. Despite this deficiency, no virus was observed by plaque assay at day 8 postinfection in mutant or wild-type mice (data not shown), suggesting the presence of sufficient effector cells for viral control. Based on this result, we conclude that ETAA1 deficiency, either by loss of almost all the protein or by deletion of amino acids 78–119, results in a specific immune deficiency that preserves circulating T-cell numbers but cripples their clonal expansion after infection or immunization.

ETAA1 Deficiency Interferes with T-Cell Clonal Expansion Cell Autonomously. Competitive bone marrow transplants were performed to examine whether the immunologic effects of ETAA1 deficiency were T-cell intrinsic or secondary to abnormalities in other cells within or outside the blood system. C57BL/6 $Rag1^{-/-}$ mice, which lack T or B cells, were transplanted with an equal mixture of bone marrow from $Etaa1^{\Delta Ex2/\Delta Ex2}$ $CD45.2^+$ C57BL/6 mice and from $Etaa1^{+/+}$ C57BL/6 mice bearing a congenic CD45.1 cell surface marker. In parallel, control mixed BM chimeras were transplanted with an equal mixture of bone marrow from $Etaa1^{+/+}$ $CD45.2^+$ and $Etaa1^{+/+}$ $CD45.1^+$ mice, so that the competing transplanted cells had normal ETAA1. In competition with wild-type $CD45.1^+$ hematopoietic progenitors and lymphocytes, $CD45.2^+$ cells with normal ETAA1 accounted for ∼50% of lymphocytes, B cells, and naïve T cells in the reconstituted control chimeras, whereas ETAA1-deficient $CD45.2^+$ cells reconstituted ∼30% of the same lymphocyte compartments (Fig. 2*A*). In contrast, ETAA1-deficient $CD45.2^+$ cells did not contribute to the $KLRG1^{hi}$ effector $CD4^+$ or $CD8^+$ T cells in blood at 2 wk weeks after immunization (even after normalizing for the poorer ETAA1-deficient lymphocyte reconstitution), despite the formation of many effector T cells from the wild-type $CD45.1^+$ cells in the same animals (Fig. 2 *B* and *C*). In control mixed chimeras analyzed in parallel, $CD45.2^+$ cells with wild-type ETAA1 formed effector T cells at only slightly less frequency than their $CD45.1^+$ competitors (Fig. 2 *B* and *C*). These results demonstrate that ETAA1 deficiency acts cell-autonomously within T cells to profoundly cripple effector T-cell formation.

To extend this analysis to other subsets of antigen-induced T and B cells, the mixed chimeras were immunized with sheep red blood cells (SRBCs) to elicit germinal center (GC) reactions in the spleen composed of rapidly dividing GC B cells and T follicular helper (T_{FH}) cells. Although large numbers of both subsets were formed in each chimeric animal, they were derived mostly from wild-type cells; even after normalizing for their slightly diminished contribution to B cells and CD4 naïve T cells, ETAA1-deficient $CD45.2^+$ cells accounted for only 30% of the GC B cells and 6% of T_{FH} cells (Fig. 2*D*). In control chimeras, $CD45.2^+$ cells with wild-type ETAA1 accounted for 50% of the GC B cells and T_{FH} cells (Fig. 2*D*; also normalized for reconstitution). Thus, ETAA1 deficiency also acts cell-autonomously to profoundly compromise T_{FH} cell formation, and has only a modest cell-autonomous effect on GC B-cell accumulation.

The cell-autonomous effect of ETAA1 deficiency also was demonstrated at the level of antigen-specific T cells by infecting mixed bone marrow chimeras with LCMV-Arm and measuring the contribution of $CD45.2^+$ cells to tetramer-binding $CD8^+$ and $CD4^+$ T cells at day 8 postinfection. Again, a profound and specific deficiency in antigen-specific T-cell accumulation was observed in ETAA1-deficient $CD45.2^+$ cells, but not in wild-type $CD45.2^+$ cells, in control mixed chimeras (Fig. 2*E*). A similar decrease in effector cell number was observed when antigen-specific T cells were enumerated by peptide-stimulated IFN-γ expression.

Partial Embryonic Lethality and Smaller Body Size in ETAA1-Deficient Mice. Two significant observations were made during further breeding of *Etaa1* mutant heterozygotes and homozygotes: (*i*) $Etaa1^{\Delta Ex2/\Delta Ex2}$ homozygous male mice had comparable fecundity to wild-type C57BL/6 mice (Fig. 3*A*; the fecundity of homozygous females was not assessed), and (*ii*) homozygous mutant mice were born at a lower frequency than expected (Table 1). In $Etaa1^{\Delta Ex2/+} \times Etaa1^{\Delta Ex2/+}$ mouse crosses, only 6.8% of offspring were homozygous mutants, rather than the expected 25%. A similarly decrease was seen in the the frequency of homozygous mutants born from intercrosses of $Etaa1^{C166X/+}$ mice (Table 1). In $Etaa1^{\Delta Ex2/\Delta Ex2} \times Etaa1^{\Delta Ex2/+}$ crosses, homozygous mutant mice were born at a 20% frequency instead of the expected 50%. Thus, ETAA1 deficiency appears to result in partially penetrant embryonic lethality. Nevertheless, $Etaa1^{\Delta Ex2/\Delta Ex2}$ homozygous embryos were present at the expected rate at embryonic day 12 (Table 1), indicating that homozygous lethality occurs after this stage of development, in contrast to the blastocyst-stage lethality caused by homozygous null mutations in *Rpa1*, *Atr*, and *Topbp1* (9–13).

Along with being fertile, homozygous mutant mice that were born lacked discernable pathology. Homozygotes had slightly decreased mean body weight and length, with decreased body mass index (BMI) evident in older mice (Fig. 3*B*). In a cohort of mice aged >1 y, there was no evidence of increased mortality in the $Etaa1^{\Delta Ex2/\Delta Ex2}$ homozygous mice (Fig. 3*C*), and a comprehensive pathological analysis of these mice failed to reveal any obvious abnormality (*SI Appendix*). T-cell developmental subsets were

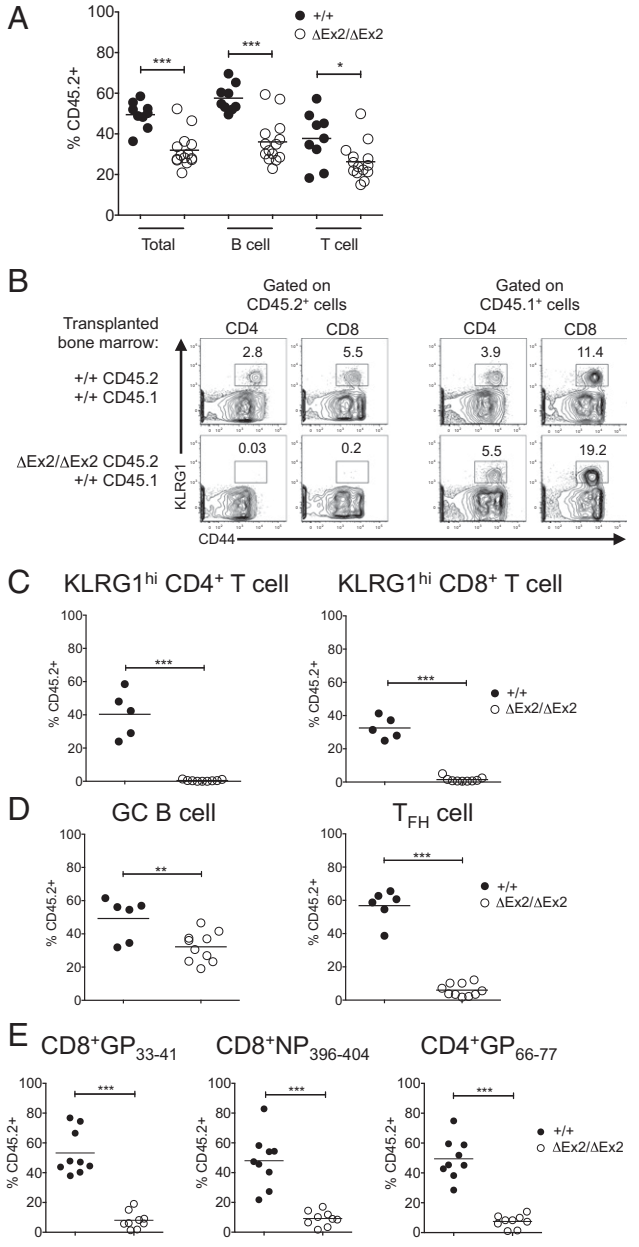

Fig. 2. *Etaa1* control of effector T-cell expansion is cell intrinsic. *Rag1*$^{-/-}$ mice were lethally irradiated and reconstituted with a 50:50 mixture of CD45.1$^+$ wild-type bone marrow and CD45.2$^+$ *Etaa1*$^{+/+}$ or *Etaa1*$^{\Delta Ex2/\Delta Ex2}$ bone marrow. (*A*) Contributions of CD45.2$^+$ *Etaa1*$^{+/+}$ and *Etaa1*$^{\Delta Ex2/\Delta Ex2}$ cells to total lymphocytes, B cells, and T cells in competitive mixed bone marrow chimeras, measured in blood before immunization or infection. (*B* and *C*) Wild-type and mutant mixed bone marrow chimeras were immunized with CGG and inactivated *B. pertussis*, and blood was analyzed at day 28 postimmunization. (*B*) Representative plots showing the percentage of CD45.2$^+$ and CD45.1$^+$ cells falling within the KLRG1^{hi} effector T-cell gate. (*C*) %CD45.2$^+$ cells among all KLRG1^{hi} effector T cells in individual wild-type or mutant mixed bone marrow chimeras. To correct for individual differences in overall reconstitution by CD45.2$^+$ marrow in *A*, each postimmunization value was normalized to the %CD45.2$^+$ cells among all CD4 or CD8 cells in the same chimeric mouse before immunization. (*D*) %CD45.2$^+$ cells within germinal center B cells (GC; B220$^+$GL-7$^+$CD95$^+$) and T_{FH} cells (CD4$^+$PD-1^{hi}CXCR5^{hi}) in the spleen on day 7 postimmunization with SRBCs, normalized to the %CD45.2$^+$ cells in all B cells or to the CD4 T cells in the same chimera before immunization. (*E*) %CD45.2$^+$ splenic cells within the CD8$^+$GP$_{33-41}$, CD8$^+$NP$_{396-404}$, and CD4$^+$GP$_{66-77}$ tetramer-positive cells at day 8 postinfection with LCMV-Arm in either wild-type or mutant mixed bone marrow chimeras, normalized to the %CD45.2$^+$ cells among all CD8 cells in the same chimera before infection. ***$P < 0.001$, **$P < 0.01$, *t* test.

present in normal numbers in the thymus of mutant mice, and there were normal numbers of peripheral T-cell subsets (Fig. 3*D*). Thus, the only striking abnormality caused by ETAA1 deficiency in adult mice is the profound failure to accumulate effector T cells.

ETAA1-Deficient T Cells Differentiate into Effectors Despite Poor Clonal Expansion. The diminished accumulation of antigen-specific T cells after systemic infection with LCMV (Figs. 1 and 2) also occurred when ETAA1-deficient mice were infected with herpes simplex virus type 1 (HSV1) by tattoo inoculation of shaved flank skin (24) (Fig. 4 *A* and *B*). Nonetheless, ETAA1-deficient mice displayed normal control of HSV1 in the skin and in the nervous system, as shown by lack of neurologic symptoms and typical-sized lesions at primary and secondary skin sites (Fig. 4*C*). Because effector T cells are required to control HSV1 (25, 26), the smaller populations of effector T cells (Fig. 4 *A* and *B*) nevertheless appear to be active in vivo.

As noted above, the diminished effector T-cell population in LCMV-infected ETAA1-deficient mice appeared sufficient to clear infection by day 8 postinfection. Detailed flow cytometry phenotyping of the LCMV tetramer-specific CD8$^+$ T cells at this timepoint revealed that the effector CD8$^+$ T cells that did form exhibited relatively normal effector differentiation despite some alterations in effector subset composition (Fig. 5 *A*–*D*); in fact, if anything the mutant cells had slightly greater effector function, as evidenced by slightly elevated production of IFN-γ and granzyme B (GzmB). Similarly, the effector CD4$^+$ T cells that formed exhibited normal subset differentiation (27) except for a slight decrease in PSGL1^{lo} T_{FH} cells (Fig. 5*E*). Cytokine function also was normal in these effector CD4$^+$ T cells, again with slightly enhanced cytokine function within mutant effectors.

ETAA1-Deficient T Cells Proliferate Normally in Vitro and in Vivo. To understand why a smaller population of effector T cells was formed from ETAA1-deficient precursors, we needed to track the preceding phase of naïve T-cell activation and division at early time points after virus infection. To track CD8$^+$ T cells bearing a defined T-cell receptor (TCR) for virus antigen, we crossed the *Etaa1*$^{\Delta Ex2}$ allele to congenically marked (CD45.1$^+$) P14 TCR transgenic C57BL/6 mice, which express a TCR specific for LCMV GP$_{33-41}$ antigen. Naïve CD8$^+$ T cells expressing the P14 TCR developed and accumulated normally despite ETAA1 deficiency. We then transferred 5 × 10^4 *Etaa1*$^{+/+}$ or *Etaa1*$^{\Delta Ex2/\Delta Ex2}$ CD45.1$^+$ P14 CD8$^+$ T cells into CD45.2$^+$ C57BL/6 mice with normal ETAA1, and infected the recipients with LCMV-Arm. Despite having the same starting naïve P14 precursor frequency, 10-fold fewer mutant than wild-type P14 CD8$^+$ T-cell progeny accumulated in the spleen by day 5 postinfection, and 100-fold fewer accumulated by day 8 (Fig. 6*A*). Importantly, the decrease in the number of mutant P14 cells observed within the spleen was not due to migration to other organs, given that similar deficiencies in mutant P14 cell numbers were seen in the lymph nodes, bone marrow, lung, and liver (Fig. 6*B*).

These results indicate that the decreased clonal expansion of ETAA1-deficient T cells was related either to decreased T-cell division or to decreased survival of the dividing progeny. We first examined T-cell division and survival in vitro after stimulation. Polyclonal T cells from the spleen of CD45.2$^+$ *Etaa1*$^{\Delta Ex2/\Delta Ex2}$ mice or CD45.1$^+$ wild-type controls were labeled with the division-tracking dye Cell Trace Violet (CTV) and stimulated with anti-CD3 for 3–4 d. Strikingly, the mutant T cells exhibited normal cell division after stimulation, with similar results obtained over a range of anti-CD3 doses with or without anti-CD28 (Fig. 6*C*). To test in vitro proliferative capacity following antigen-specific stimulation, we stimulated *Etaa1*$^{+/+}$ or *Etaa1*$^{\Delta Ex2/\Delta Ex2}$ P14 CD8$^+$ T cells with GP$_{33-41}$ peptide and IL-2 in vitro and analyzed them daily for 5 d. ETAA1-deficient P14 cells acquired the Ki67 cell cycle marker and increased in number comparably to their wild-type counterparts, and also exhibited a comparable percentage of viable cells at each time point (Fig. 6*D*), demonstrating that ETAA1 is dispensable for clonal expansion in vitro.

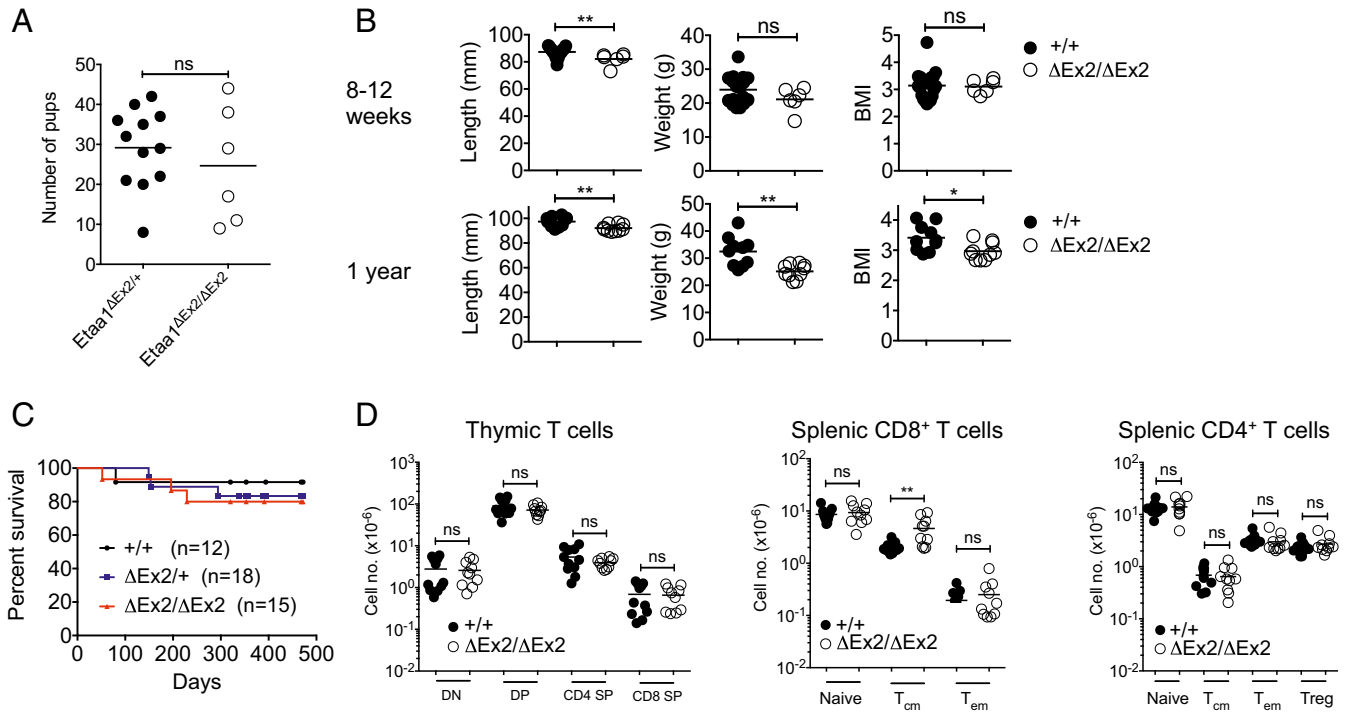

Fig. 3. *Etaa1*-deficient mice display little or no steady-state phenotype. (*A*) Fecundity of male $Etaa1^{\Delta Ex2/\Delta Ex2}$ mice vs. male $Etaa1^{\Delta Ex2/+}$ controls, expressed as the number of pups sired per male over a 6-mo period. (*B*) Length, weight, and BMI of young (8–12 wk) or old (1 y) $Etaa1^{+/+}$ or $Etaa1^{\Delta Ex2/\Delta Ex2}$ mice. (*C*) Survival curves of $Etaa1^{+/+}$, $Etaa1^{\Delta Ex2/+}$, and $Etaa1^{\Delta Ex2/\Delta Ex2}$ mice. (*D*) Numbers of thymic (*Left*) and splenic (*Right*) T-cell subsets, defined as follows: double-negative (DN), $B220^{-}CD4^{-}CD8^{-}$; double-positive (DP), $B220^{-}CD4^{+}CD8^{+}$; CD4 single-positive (SP), $B220^{-}CD4^{+}CD8^{-}$; CD8 SP, $B220^{-}CD4^{-}CD8^{+}$; naïve, $CD4^{+}$ or $CD8^{+}$ and $CD62L^{hi}CD44^{lo}$; T_{cm}, $CD4^{+}$ or $CD8^{+}$ and $CD62L^{hi}CD44^{hi}$; T_{em} (or effector), $CD4^{+}$ or $CD8^{+}$ and $CD62L^{lo}CD44^{hi}$; and Treg, $CD4^{+}Foxp3^{+}CD25^{int\text{-}hi}$. $^{**}P < 0.01$; $^{*}P < 0.05$; ns, not significant by *t* test.

These experiments showed that ETAA1-deficient T cells divide normally in tissue culture. We next tested whether ETAA-deficient T cells divide normally in vivo, by CTV-labeling naïve $CD45.1^{+}$ $Etaa1^{+/+}$ and $Etaa1^{\Delta Ex2/\Delta Ex2}$ P14 $CD8^{+}$ T cells before injecting them into the circulation of wild-type $CD45.2^{+}$ C57BL/6 mice that were subsequently infected with LCMV-Arm. When CTV dilution was analyzed in $CD45.1^{+}$ $CD8^{+}$ T cells in the spleen at 60 h after infection, the same proportion of P14 cells had divided whether they were ETAA1-deficient or wild-type, and those cells that had divided exhibited a similar CTV mean fluorescence intensity (MFI) (Fig. 6*E*). Although CTV was completely diluted from all P14 cells by day 5 postinfection, there were comparable percentages of $Ki67^{+}$ cells in cycle (Fig. 6*F*) despite the 10-fold reduction in mutant P14 numbers at this time point (Fig. 6*A*). Determination of the proportion of P14 cells that were dead and/or apoptotic at this time point by flow cytometry using Annexin V and fixable live/dead dye staining revealed no consistent difference despite a variable trend toward slightly more death within mutant cells. Given that cell death in vivo can be difficult to detect due to rapid apoptotic cell clearance, the normal division observed in these experiments favor the conclusion that ETAA1-deficient T cells have decreased clonal expansion due to impaired survival of dividing progeny.

ETAA1-Deficient T Cells Accumulate Elevated Levels of DNA Damage. We performed gene expression analysis by RNA sequencing (RNA-seq) to test for differences that might explain why ETAA1-deficient dividing P14 T cells have diminished survival during their proliferative response to viral antigen in infected mice. As above, $Etaa1^{+/+}$ or $Etaa1^{\Delta Ex2/\Delta Ex2}$ $CD45.1^{+}$ P14 cells were injected into wild-type C57BL/6 mice and the recipients infected with LCMV. $CD45.1^{+}$ $CD8^{+}$ P14 progeny were purified from the spleen by fluorescence activated cell sorting on day 5 postinfection, when the clonal expansion defect first becomes evident. cDNA libraries from four pools of sorted mutant or wild-type P14 cells, isolated from independent sets of recipient mice, were analyzed by massively parallel RNA-seq. Using edgeR (28), 109 differentially expressed genes were identified, including 94 that were increased in mutant P14 cells compared with wild-type (Table S1). Gene set enrichment analysis (GSEA) (29) of the RNA-seq data indicated that the gene set of TP53 (p53)-induced genes was significantly enriched within up-regulated mRNAs in mutant cells (Fig. 7*A*). Gene Ontology (GO)/Kyoto Encyclopedia of Genes and Genomes (KEGG) enrichment analysis of the 94 genes up-regulated in mutant cells using g:Profiler (30) yielded strong evidence of up-regulation of p53-linked genes, particularly genes associated with p53-mediated apoptosis and also genes generally associated with

Table 1. Frequencies of *Etaa1*-deficient mouse strain genotypes

Cross	WT	Heterozygote	Mutation	*P* value
$\Delta Ex2/^{+} \times \Delta Ex2/^{+}$	32.5% (326/1,002)	60.7% (608/1,002)	6.8% (68/1,002)	< 0.0001
$\Delta Ex2/^{+} \times \Delta Ex2/\Delta Ex2$	NA	79.7% (126/158)	20.3% (32/158)	< 0.0001
$\Delta Ex2/^{+} \times \Delta Ex2/^{+}$ (E12 embryos)	25.5% (25/98)	52% (51/98)	22.5% (22/98)	0.9385
$C166X/^{+} \times C166X/^{+}$	32.5% (53/163)	62.6% (102/163)	4.9% (8/163)	< 0.0001

NA, not applicable.

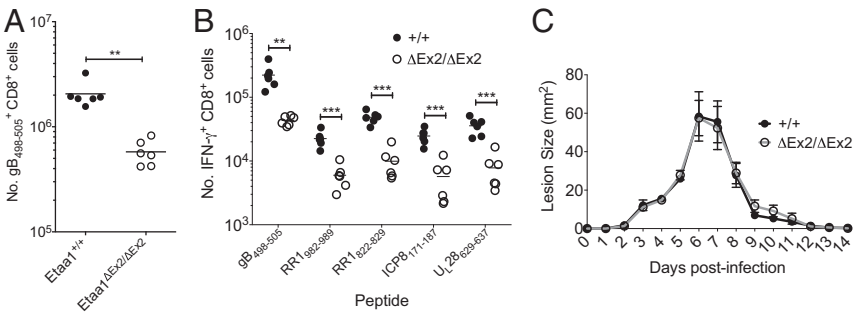

Fig. 4. *Etaa1*-deficient mice exhibit defective T-cell responses to HSV1 infection. *Etaa1*$^{+/+}$ or *Etaa1*$^{\Delta Ex2/\Delta Ex2}$ mice were infected on the flank with HSV1. (*A* and *B*) At day 19 postinfection, splenic CD8$^+$gB498–505$^+$ dextramer cells, or IFN-γ$^+$ CD8$^+$ cells identified after stimulation with the listed peptides, were enumerated. (*C*) Mean ± SEM size of the flank lesion over the course of infection (n = 6). ***P < 0.001, **P < 0.01, t test.

apoptosis pathways (Table 2). Independently, p53-binding sites were significantly enriched within the genes up-regulated in *Etaa1*$^{\Delta Ex2/\Delta Ex2}$ P14 cells (Table S2).

Because TP53 activity is induced by DNA replication stress and DNA damage, accompanied by ATR or ATM kinase activation, we used flow cytometry to measure Ser139-phosphorylated H2AX (γH2AX) within mutant and wild-type P14 cells proliferating in LCMV-infected recipient mice. ETAA1-deficient P14 CD45.1$^+$ CD8$^+$ T effector cells had increased γH2AX staining relative to wild-type control P14 cells on both day 5 and day 8 postinfection (Fig. 7 *B* and *C*). In contrast, when P14 cells were stimulated to divide in tissue culture, using the conditions and time points above that showed no decrease in P14 accumulation in vitro, there was no evidence of increased γH2AX staining within mutant P14 T cells. Thus, ETAA1 deficiency causes a selective decrease in the survival of dividing T cells in vivo, but not in tissue culture, that is correlated with increased phosphorylation of ATR/ATM substrates in vivo, but not in tissue culture.

Discussion

Here we identify a specific immune response function for ETAA1, which was an obscure pioneer protein at the time that we initiated and performed these studies. ETAA1's immunological function was revealed by a genetic screening strategy that merges elements of forward (phenotype-driven) genetics and reverse (gene-driven) genetics. Randomly induced mutations in the mouse germ line were identified by exome sequencing before phenotypic screening, so that breeding and phenotyping could focus on prioritized mutations with possible immune effects based on gene expression patterns or other systems-level information. Our analysis of mouse mutants with a null allele or an exon 2 deletion allele indicates that in adult animals, ETAA1 is selectively required to suppress the DNA damage response in rapidly proliferating effector T cells during an immune response. These immunologic findings are complemented by four papers published at the end of 2016 identifying ETAA1 as a functional component of the ATR-activating replication stress response complex in human cancer cell lines, with exon 2 encoding the ATR-activating domain of ETAA1 (18–21). This advance represents a striking demonstration that specific, rate-limiting pathways are needed to insulate proliferating effector T cells against replication stress that might be targeted for suppression of transplant rejection, graft-vs.-host disease, and autoimmune disease.

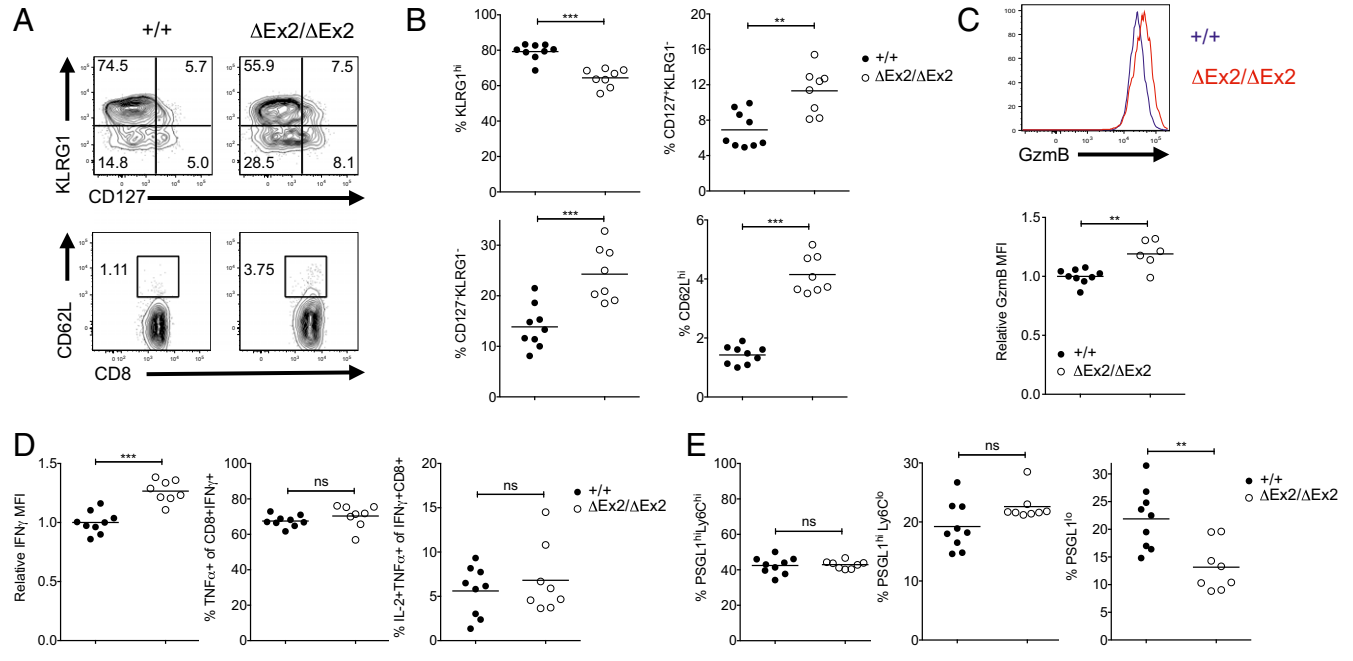

Fig. 5. *Etaa1*-deficient T cells differentiate into functional effector cells. *Etaa1*$^{+/+}$ and *Etaa1*$^{\Delta Ex2/\Delta Ex2}$ mice were infected with LCMV-Arm, and at day 8 postinfection either CD8$^+$GP$_{33–41}$ (*A–D*) or CD4$^+$GP$_{66–77}$ (*E*) tetramer-positive cells were assessed for short-lived effector (CD127^{lo}KLRG1^{hi}) and memory precursor (CD127^{hi}KLRG1^{lo} and potentially CD62L$^{int\text{-}hi}$) markers (*A* and *B*), effector function (GzmB expression and IFN-γ, TNFα, and IL-2 production) (*C* and *D*), and T$_{H1}$ (PSGL1^{hi}Ly6C^{hi}), CD4 memory precursor (PSGL1^{hi}Ly6C^{lo}) and T$_{FH}$ (PSGL1^{lo}) differentiation (*E*). ***P < 0.001; **P < 0.01; ns, not significant, t test.

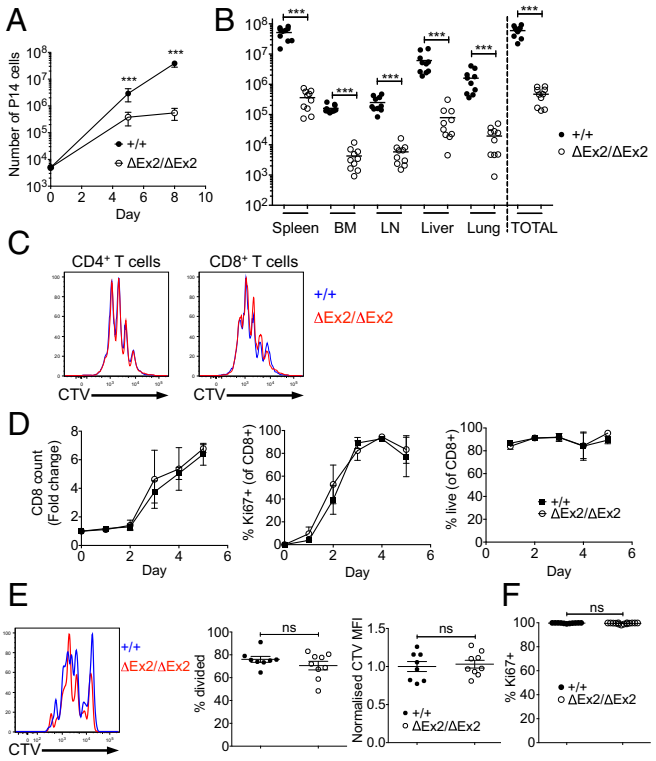

Fig. 6. *Etaa1*-deficient T cells exhibit normal proliferation and tissue migration. (*A* and *B*) CD45.2$^+$ C57BL/6 mice were injected i.v. with 5×10^4 CD45.1$^+$ *Etaa1*$^{+/+}$ or *Etaa1*$^{\Delta Ex2/\Delta Ex2}$ P14 cells before infection with LCMV-Arm. (*A*) Splenic P14 cells enumerated at days 5 and 8 postinfection showing mean and SD (n = 10–14/group). (*B*) P14 numbers in the indicated tissues on day 8 postinfection (*C*) CD45.1$^+$ wild-type and CD45.2$^+$ *Etaa1*$^{\Delta Ex2/\Delta Ex2}$ splenocytes were mixed in a 50:50 ratio, labeled with CTV, and stimulated with 1 μg/mL anti-CD3. Then 3–4 d later, CTV dilution in CD4$^+$ and CD8$^+$ T cells from wild-type (CD45.1$^+$) and mutant (CD45.2$^+$) cells was compared. (*D*) *Etaa1*$^{+/+}$ and *Etaa1*$^{\Delta Ex2/\Delta Ex2}$ P14 cells were stimulated in vitro with GP_{33-41} peptide and IL-2, live P14 cells were enumerated (expressed as fold change over starting cell number), and Ki67 expression and viability (% 7AAD$^-$ Live/Dead dye$^-$) were measured by flow cytometry at each timepoint. (*E*) CD45.2$^+$ C57BL/6 mice were injected i.v. with 8×10^5 CTV-labeled CD45.1$^+$ *Etaa1*$^{+/+}$ or *Etaa1*$^{\Delta Ex2/\Delta Ex2}$ P14 cells before infection with LCMV-Arm. At day 2.5 postinfection, CTV dilution in the transferred P14 cells was measured by flow cytometry, with the CTV MFI in divided P14 cells from each mouse normalized to the average MFI in wild-type P14 cells in the same experiment. Data are pooled from two experiments. (*F*) The percentage of Ki67$^+$ P14 cells at day 5 postinfection in the experiment outlined in *A* and *B*. ***$P < 0.001$; ns, not significant, two-way ANOVA (*A*) or *t* test (*B*, *E*, and *F*).

The pattern of *Etaa1* mRNA expression on BioGPS (15) was the primary a priori evidence suggesting a possible immune system function, and this pattern is broadly consistent with the effects seen in homozygous mutant mice. *Etaa1* mRNA is highest in embryonic stem cells, consistent with the observed partial embryonic lethality, although lethality occurs after embryonic day 12. *Etaa1* is next most highly expressed in T and B lymphocytes, consistent with the observed profound decrease in effector T-cell accumulation. Aside from a subtle decrease in body size, homozygous mice that were born did not display any tissue pathology or increased mortality, were fertile, and males successfully sired multiple litters of offspring. Within the immune system, *Etaa1* mRNA is nevertheless expressed at comparable levels in many subsets of developing, mature, and activated T, B, natural killer, and dendritic cells and also in hematopoietic stem and progenitor cells (probeset 10384486; www.immgen.org/) (31), yet surprisingly the effects of ETAA1 deficiency were restricted to mature T cells after they had been activated by antigen and had started to rapidly divide in vivo. Earlier stages of blood cell progenitor and T-cell and B-cell progenitor proliferation in the thymus and bone marrow, and naïve T-cell and B-cell accumulation in the blood and spleen, were largely unaffected by ETAA1 deficiency in homozygous mutant mice and in competitive mixed bone marrow transplants. In contrast to the profound cell-autonomous decrease in ETAA1-deficient T_{FH} cell accumulation in immunized mixed bone marrow chimeras, accumulation of ETAA1-deficient GC B cells in the same chimeras displayed only a subtle cell-autonomous decrease.

Within rapidly dividing T cells responding to virus infection in vivo, we delineated the effect of ETAA1 deficiency by showing that it does not diminish their rate of division or differentiation, but increases their levels of Ser-139 phosphorylated H2AX and expression of TP53-induced mRNAs. As discussed below, this finding directly aligns with the recently published identification of a biochemical function for ETAA1 as an activator of ATR kinase and the replication stress response in human cancer cell lines (18–21).

During DNA replication, unwinding by MCM family DNA helicases exposes the leading and lagging strands as ssDNA, which are bound and prevented from reannealing by RPA proteins. Tight regulation is required to ensure that both strands of ssDNA are converted into dsDNA by replicase complexes at the same pace as the helicase unwinds unreplicated DNA. The master regulator is ATR kinase, and, consequently, ATR genetic deficiency in mice results in completely penetrant embryonic lethality and failure of inner mass cell proliferation at the blastocyst stage (9, 10). Partial loss of function *ATR* mutations causes Seckel syndrome in humans and a similar condition when introduced into mice (12), characterized by microcephaly, dwarfism, bone marrow failure, and (in mice) incompletely penetrant embryonic lethality. ATR is recruited to replication forks by its association with ATR-Interacting Protein (ATRIP), which binds to RPA on ssDNA. Phosphorylation by ATR is activated if there is replication stress causing the replication fork to collapse or stall. Replication stress can arise from factors as simple as deoxyribonucleotide shortage, which can be

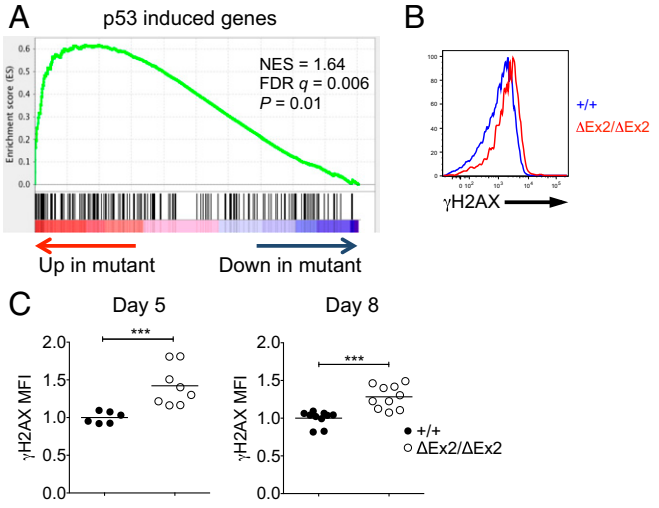

Fig. 7. *Etaa1*-deficient T cells have an enhanced DNA damage response. CD45.2$^+$ C57BL/6 mice were injected i.v. with 5×10^4 CD45.1$^+$ *Etaa1*$^{+/+}$ or *Etaa1*$^{\Delta Ex2/\Delta Ex2}$ P14 cells before infection with LCMV-Arm. (*A*) The *Etaa1*$^{+/+}$ and *Etaa1*$^{\Delta Ex2/\Delta Ex2}$ P14 cells were sorted at day 5 postinfection, and gene expression was analyzed by RNA-seq. The plot shows GSEA demonstrating a significant up-regulation of the p53 (TP53)-induced genes within the ranked RNA-seq data (ordered from most up-regulated to most down-regulated in mutant vs. wild-type cells). NES, normalized enrichment score; FDR *q*, false discovery rate *q* score. (*B* and *C*) Representative and compiled data of γH2AX staining within *Etaa1*$^{+/+}$ and *Etaa1*$^{\Delta Ex2/\Delta Ex2}$ P14 cells at day 5 (*B* and *C*) and day 8 (*C*) postinfection ***$P < 0.001$, *t* test.

Table 2. GO/KEGG terms enriched in genes up-regulated within *Etaa1*$^{\Delta Ex2/\Delta Ex2}$ P14 cells

GO/KEGG term	GO/KEGG ID	*P* value
p53-signaling pathway	KEGG: 04115	0.00000231
Positive regulation of cellular metabolic process	GO: 0031325	0.0000114
Positive regulation of macromolecule metabolic process	GO: 0010604	0.0000129
Cytokine–cytokine receptor interaction	KEGG: 04060	0.0000261
Positive regulation of metabolic process	GO: 0009893	0.0000391
Positive regulation of cellular process	GO: 0048522	0.000105
Positive regulation of programmed cell death	GO: 0043068	0.00018
Positive regulation of cell death	GO: 0010942	0.000308
Response to external stimulus	GO: 0009605	0.000343
Cell activation	GO: 0001775	0.000461
Positive regulation of biological process	GO: 0048518	0.000469
Intrinsic apoptotic signaling pathway by p53 class mediator	GO: 0072332	0.000476
Leukocyte activation	GO: 0045321	0.000532
Positive regulation of protein metabolic process	GO: 0051247	0.000666
Apoptotic signaling pathway	GO: 0097190	0.000846
Positive regulation of nucleic acid-templated transcription	GO: 1903508	0.00122
Positive regulation of transcription, DNA-templated	GO: 0045893	0.00122
Regulation of apoptotic process	GO: 0042981	0.00123

experimentally or clinically induced by inhibiting ribonucleotide reductase with the drug hydroxyurea. Replication stress also can arise when the replicase encounters DNA damage; for example, single-strand nicks created by the DNA torsion-releasing activity of Topoisomerase 1 upstream of the helicase, which fail to be repaired in the presence of the anticancer drug camptothecin and result in dsDNA breaks if the replication fork collides with the nick.

During physiological replication stress, collapsed forks release the replicase complex and expose junctions between ssDNA and replicated dsDNA that recruit the PCNA-like Rad9-Rad1-Hus1 (9-1-1) protein complex. The 9-1-1 complex together with other proteins recruits TOPBP1, and TOPBP1 contains an ATR-activating domain with a critical residue, W1147, that binds ATR and stimulates its kinase activity (32). TOPBP1 appears to be the primary ATR activator under physiological mammalian cell replication, because homozygous null mutations or W1147 point mutations in mice result in early embryonic lethality at the blastocyst stage, phenocopying null mutations in *Atr* (11, 33).

The recent studies of ETAA1 in human cancer cell lines reveal that ETAA1 serves as an activator of ATR in parallel with TOPBP1 (18–21), but likely acts primarily at stalled replication forks with extended ssDNA segments coated by RPA that are too distant to the ssDNA-dsDNA replication junctions for TOPBP1 recruitment. The studies identify RPA-binding domains in the middle and C terminus of ETAA1, and an ATR activation domain in the N terminus encoded by exon 2 and containing a critical W107 residue (corresponding to W109 in mouse). Cancer cell lines lacking ETAA1 had normal rates of cell division but in some but not other cancer lines the loss of ETAA1 resulted in slower and assymetrical progress of replication forks from sites of initiation and slightly increased H2AX Ser139 phosphorylation (18–21). These biochemical phenotypes of ETAA1-deficient cancer cells were greatly exaggerated by increasing replication stress with hydroxyurea or camptothecin, resulting in overt loss of cell viability. Combined treatment with hydroxyurea to inhibit replicase, and drugs to inhibit ATR, trigger replication fork breakage resulting in dsDNA breaks that activate the related protein kinase, Ataxia Telangiectasia Mutated (ATM), to phosphorylate H2AX and induce TP53. Thus, ATM activation by dsDNA breaks also may account for the increased H2AX in ETAA1-deficient cancer cell lines and in effector T cells in vivo, as well as the induction of TP53-response genes in effector T cells. The cancer cell phenotypes were equally severe when the cells were engineered to have a point mutation in the ETAA1 exon 2 splice acceptor, so that exon 2 was skipped to delete 42 amino acids from the ATR-activating domain including W107, despite the cells' production of normal amounts of RPA-binding ETAA1 (18). These results provide a biochemical explanation for the equally severe effector T-cell deficiency observed here in mice with an exon 2 skipping mutation or a truncating null mutation. Although we have not confirmed that the exon 2 deleted protein is made in mouse T cells, as is the case in human cell lines with an exon 2 skipping mutation (18), it nevertheless is reasonable to infer from these results that ATR activation is the critical function provided by ETAA1 in rapidly dividing T cells in vivo.

Given the evidence that ETAA1 and TOPBP1 work in parallel and cooperatively to activate ATR in cancer cells in tissue culture, it is surprising that a homozygous ETAA1 deficiency in mice did not produce the fully penetrant early embryonic lethality caused by TOPBP1 or ATR deficiency. Unlike ATR and TOPBP1 deficiency, homozygous lethality occurred after embryonic day 12 in ETAA1-mutant embryos, indicating a relatively late block in development. Even when ATR is conditionally inactivated in a subset of cells in adult mice, it causes profound depression of bone marrow and thymus cellularity and graying of hair, along with selective loss of ATR-deficient cells from bone marrow and thymus, in chimeric animals (34); however, these parameters were relatively normal in ETAA1-deficient mice and mixed bone marrow chimeras. TOPBP1 conditional deletion in developing B or T cells results in almost complete absence of pre-B and mature B cells and greatly decreased numbers of DP and SP thymocytes and mature T cells (35), whereas B-cell and T-cell development was at most only slightly decreased in ETAA1-deficient mice only under competitive repopulation conditions.

Perhaps the closest parallel to the phenotype of mice with ETAA1 deficiency is with mice homozygous for the ATR partial loss-of-function Seckel mutation (12). *Atr*^{seckel} homozygous mice were born at one-half the expected frequency, similar to the incompletely penetrant embryonic lethality in ETAA1-deficient mice. However, adult *Atr*^{seckel} homozygotes were microcephalic, micrognathic, and dwarf (only one-third the weight of their wild-type siblings), whereas ETAA1-deficient mice exhibited 90% of the weight and length of wild-type controls with a normal cranial appearance. *Atr*^{seckel} homozygotes have increased numbers of cells with phosphorylated H2AX foci and TP53 induction in histological sections throughout E13.5 embryos, consistent with exaggerated replicative stress, although this was not apparent in tissues from adult mutant mice, including brain, colon, proliferating B cells, stomach, liver, and lung. The adult *Atr*^{seckel} homozygotes died within 6 mo and exhibited severe pancytopenia, whereas ETAA1-deficient mice showed no apparent increase in mortality and normal blood cells. Considered together with the loss of ATR-deficient marrow cells in adult chimeric animals (34), ETAA1 appears to not be the rate-limiting activator for ATR during the rapid cell division of adult hematopoiesis and lymphopoiesis.

One of the most important questions raised by our data is why ETAA1 regulates replication stress under such restricted and specific circumstances in dividing effector T cells in vivo, but not in vitro. The simplest explanation is that ETAA1 becomes rate-limiting for ATR activation only in cells that proliferate exceptionally rapidly; in all other situations, *Topbp1* can compensate for *Etaa1* loss. Effector T cells proliferate in vivo at a much faster rate compared with T cells in vitro, and in fact have one of the fastest proliferation rates recorded (3). Interestingly, the only other cell type reported to proliferate at a rate comparable to effector T cells in vivo are dividing cells during mouse embryonic

development (3, 36), and indeed the only other phenotype observed in *Etaa1*-deficient mice is partial embryonic lethality.

Our findings have several clinical implications. Given the selective phenotype observed in *Etaa1*-deficient mice, it is possible that *ETAA1* mutations in humans cause selective deficiency of effector T cells that might have a nonsyndromic clinical presentation of variable opportunistic infections. Indeed, a previous statistical association between human *ETAA1* polymorphisms and the risk of pancreatic cancer (37) could be related as much to compromised immunosurveillance downstream of impaired ETAA1 protein function as to increased cellular transformation due to genomic instability. Furthermore, given the selective phenotype seen in the absence of ETAA1, transient targeting of ETAA1, or its interactions with other components of the replication stress response, may represent a novel strategy for depleting proliferating, autoreactive T cells in organ or bone marrow transplantation or in autoimmune disease. Further work is clearly needed to investigate the clinical relevance and potential of this pathway.

Methods

Mice. *Etaa1*$^{\Delta Ex2/\Delta Ex2}$ and *Etaa1*$^{C166X/C166X}$ mice were chosen from a list of random single-nucleotide variants generated by ENU mutagenesis (databases.apf.edu.au/mutations) and bred to homozygosity at generation 3 (17). C57BL/6 NCrl (C57BL/6), B6.SJL-*Ptprc*^{a} *Pepc*^{b}/BoyJ (CD45.1), and B6.129S7-*Rag1*^{tm1Mom}/J (*Rag1*$^{-/-}$) mice were purchased from the Australian Phenomics Facility. P14 transgenic animals have been described previously (38). For animal BMI studies, BMI was defined as weight in kilograms/length in meters squared. A detailed pathological analysis of tissue sections was performed by the Australian Phenomics Network Histopathology and Organ Pathology Service. All animals used in this study were cared for and used in experiments in accordance with protocols approved by the Australian National University Animal Experimentation Ethics Committee and the current guidelines from the Australian Code of Practice for the Care and Use of Animals for Scientific Purposes.

Infections, Immunizations, and Plaque Assays. Mice were infected with LCMV-Arm by i.p. injection with 2×10^5 pfu of virus. LCMV viral plaque assays were conducted as described previously (39). For HSV1 infections, mice were first anesthetized by an i.p. infection of Avertin (20 μL/g of body weight), then tattooed with HSV1 (1×10^8 pfu/mL) in a 0.5 × 0.5-cm^2 area of shaved, depilated skin on the left flank. Lesions were measured daily. CGG plus inactivated *B. pertussis* immunizations were conducted as described previously, except that CGG was not conjugated to the hapten ABA (40). CGG antibody levels were measured by ELISA on CGG-coated plates (Jackson ImmunoResearch), and were detected with an IgG1 antibody (1070-04; Southern Biotech). For SRBC immunization, mice received a 200-μL i.v. injection of 2×10^8 SRBCs (Alsevers) diluted in PBS.

Flow Cytometry Staining and Analysis. Blood was prepared for flow cytometry as described previously (16). Single-cell suspensions were prepared for flow cytometry from spleen, thymus, and lymph nodes by passing the cells through a 70-μm cell strainer. Bone marrow was prepared by flushing the bone marrow cells out of a single femur using a 26 G needle. Liver and lung cells were prepared as described previously (41). Tetramer staining and intracellular cytokine staining were performed as described previously (42, 43). For γH2AX staining, cells were first stained with LIVE/DEAD Fixable Aqua Dead Cell Stain Kit (Life Technologies) before fixation and permeabilization using the BD PhosFlow Kit (Fix Buffer I and Perm Buffer III) according to manufacturer's instructions (BD Biosciences). Cells were then stained with γH2AX antibody (clone 2F3; Biolegend), with dead cells excluded from the analysis. The following antibodies were used for staining (purchased from Biolegend unless stated otherwise): CD8α (clone 53-6.7), CD4 (clone RM4-5), CD44 (clone IM7), KLRG1 (clone 2F1), IFN-γ (clone XMG1.2), TNF-α (clone MP6-XT22), IL-2 (clone JES6-5H4), CD127 (clone A7R34), Ly6C (clone AL21; BD Biosciences), PSGL1 (clone 4RA10; BD Biosciences), CD45.1 (clone A20), CD45.2 (clone 104), CD62L (clone MEL14), Foxp3 (clone FJK-16s; eBioscience), CD25 (clone PC61), GzmB (clone GB11; Thermo Fisher Scientific), Ki67 (clone B56; BD Biosciences), B220 (clone RA3-6B2), PD-1 (clone RMP1-30), CXCR5 (clone 2G8; BD Biosciences), GL-7, and CD95 (clone Jo2; BD Biosciences). MHCI LCMV tetramers were purchased from the Biomolecular Resource Facility of the John Curtin School of Medical Research, Australian National University, and the H-2K^b/gB$_{498–505}$ dextramer was purchased from Immudex. The MHCII GP$_{66–77}$ tetramer was obtained from the National Institutes of Health's Tetramer Core Facility. Samples were acquired using an LSRII, Fortessa or X20 flow cytometer (BD Bioscience) and analyzed using FlowJo software.

Etaa1 cDNA Analysis. RNA was isolated from 2×10^6 total *Etaa1*$^{+/+}$ or *Etaa1*$^{\Delta Ex2/\Delta Ex2}$ splenocytes using the Qiagen RNeasy Kit, and cDNA was synthesized with the Invitrogen SuperScript III Reverse-Transcriptase Kit. PCR was then performed using Taq polymerase (Invitrogen) with 1.5 mM $MgCl_2$, 10% DMSO, and 0.5 μM each of the following primers: forward (exon 1 binding), 5′-AAGGAAGCATGCGGACAG-3′; reverse (exon 5 binding). 5′-TTGGATCACATCAAGTTCTTCC-3′. PCR cycling conditions were as follows: 94 °C for 3 min and then 35 cycles of 94 °C for 45 s, 56 °C for 30 s, 72 °C for 90 s, and then 72 °C for 10 min. Bands were cut out and the DNA was isolated using a Qiagen Gel Extraction Kit before submission for Sanger sequencing (using the aforementioned primers) at the Biomolecular Resource Facility of the John Curtin School of Medical Research, Australian National University.

In Vitro T-Cell Stimulation and Division Analysis. CTV (Life Technologies) labeling was performed using a final CTV concentration of 10 μM as described previously (44). For anti-CD3/CD28 stimulation, CTV-labeled CD45.1$^+$ *Etaa1*$^{+/+}$ and CD45.2$^+$ *Etaa1*$^{\Delta Ex2/\Delta Ex2}$ splenocytes were mixed in a 50:50 ratio, and 5×10^5 cells/well were stimulated in 0.1–10 μg/mL soluble anti-CD3 (clone 500A2; BD Biosciences) with or without 2 μg/mL anti-CD28 (clone 37.15; BD Biosciences) in a flat-bottom 96-well plate. For in vitro P14 stimulation, 2×10^6 P14 total splenocytes per well were cultured in a flat-bottom 24-well plate with 10 ng/mL LCMV GP$_{33–41}$ peptide (Biomolecular Resource Facility of the John Curtin School of Medical Research, Australian National University) and 10 ng/mL recombinant human IL-2 (Peprotech). Daily cell counts were normalized via expression as fold change over the starting number of CD8$^+$Vα2$^+$ P14 cells.

Transfection and Western Blot Analysis. Mouse *Etaa1* was amplified from a mouse spleen cDNA pool with Platinum *Pfx* DNA Polymerase (Thermo Fisher Scientific). The coding sequence of *Etaa1* was cloned into the pcDNA3.1$^+$ mammalian expression vector using the BamHI/XhoI sites, with the resulting clone confirmed using Sanger sequencing. For the GFP fusion protein, the *Etaa1* sequence lacking the first methionine was cloned into a pcDNA3.1$^+$ vector containing the GFP gene to generate a fusion protein. The *ΔEx2* mutant *Etaa1* sequence was generated with site-directed mutagenesis using primers that joined the first and third exons. HEK293T cells were transfected with pcDNA3.1$^+$ vectors expressing GFP-fused wild-type and *ΔEx2 Etaa1* using Lipofectamine 3000 (Thermo Fisher Scientific). Cells were harvested and lysed with sample buffer at 48 h after the transfection. Proteins were fractionated using a 4–15% Mini-PROTEAN TGX precast gel (Bio-Rad). *Etaa1* and β-actin were probed with anti-GFP and anti–β-actin antibodies (GF28R, from eBioscience, and AC-15, from Sigma-Aldrich).

Bone Marrow Chimeras. *Rag1*$^{-/-}$ recipient mice were irradiated with 5 Gy and then reconstituted with 2×10^6 bone marrow cells consisting of a 50:50 mixture of wild-type B6.CD45.1$^+$ bone marrow and B6.CD45.2+ *Etaa1*$^{+/+}$ or *Etaa1*$^{\Delta Ex2/\Delta Ex2}$ bone marrow. Mice were allowed to reconstitute for at least 8 wk before use in experiments. To account for reconstitution differences between *Etaa1*$^{+/+}$ or *Etaa1*$^{\Delta Ex2/\Delta Ex2}$ bone marrow, the %CD45.2$^+$ cells in a given lymphocyte subset measured after immunization or infection was normalized to the %CD45.2$^+$ cells in the parent subset measured in the same chimeric mouse before immunization or infection. Using LCMV tetramer-positive CD8$^+$ T cells as an example, the %CD45.2$^+$ cells in the tetramer-positive CD8$^+$ T-cell subset measured after infection was divided by the %CD45.2$^+$ cells in all CD8$^+$ T cells measured in the same mouse bled before infection, and then multiplied by 100 and divided by 2 to set the pre-infection %CD45.2$^+$ at 50%.

RNA-seq Analysis. For RNA-seq analysis, 5×10^4 CD45.1$^+$ *Etaa1*$^{+/+}$ or *Etaa1*$^{\Delta Ex2/\Delta Ex2}$ P14 cells were transferred into wild-type (CD45.2$^+$) C57BL/6 mice, followed by LCMV-Arm infection. At day 5 postinfection, CD8$^+$ CD45.1$^+$ P14 cells were isolated by fluorescence activated cell sorting, with four separate sorts conducted per genotype (i.e., eight samples total), and ~5×10^5–1×10^6 cells were recovered per sort. Total RNA was isolated using the Qiagen RNeasy Kit, and RNA-seq libraries were prepared at the Biomolecular Resource Facility, John Curtin School of Medical Research, Australian National University using the Illumina TruSeq Stranded mRNA Library Prep Kit. Samples were sequenced on an Illumina HiSeq 2500 instrument. All reads were aligned to the mouse genome reference sequence (GRCm38) using HiSat2 (45) with default parameters. Read counts were then generated for each gene in each sample using FeatureCounts (46), using annotated gene locations. Differential expression analysis was performed using edgeR (28) using a Benjamini–Hochberg adjusted *P* value threshold of 0.05 to identify significantly differentially regulated genes. GO, KEGG, and transcription factor (TF) motif enrichment analyses were performed using g:Profiler (30) based on the set

of significantly differently regulated genes identified above. GSEA (29) was conducted by searching the ranked wild-type vs. mutant RNA-seq dataset against the Hallmark Gene Sets within MSigDB using the GSEA desktop application.

Statistics. Graphs and statistical analyses were generated using Prism version 7.0 (GraphPad Software). *P* values were calculated using the two-tailed unpaired *t* test, or the two-tailed Mann–Whitney *U* test when data failed normality tests. For multiple comparisons (Fig. 1*G*), one-way ANOVA with a Tukey posttest was used, whereas two-way ANOVA was used in Fig. 6*A*. For Table 1, a χ^2 test was conducted to compare observed and expected genotype ratios.

ACKNOWLEDGMENTS. We thank the National Computational Infrastructure (Australia) for continued access to significant computation resources and technical expertise; the staff of the Australian Phenomics Facility for animal husbandry, DNA preparation, and genotyping; the staff of Australian Cancer Research Foundation Biomolecular Resource Facility for exome and Sanger sequencing; and the staff of the Microscopy and Cytometry Resource Facility for help with flow cytometry. This work was funded by National Institutes of Health Grant U19-AI100627; by the National Health and Medical Research Council through Program Grants 1016953 and 1113904, Australia Fellowship 585490, Senior Principal Research Fellowship 1081858, and C. J. Martin Early Career Fellowship 585518 (to I.A.P.); and by the National Collaborative Research Infrastructure Strategy.

1. Masopust D, Murali-Krishna K, Ahmed R (2007) Quantitating the magnitude of the lymphocytic choriomeningitis virus-specific CD8 T-cell response: It is even bigger than we thought. *J Virol* 81:2002–2011.
2. Zhang N, Bevan MJ (2011) CD8(+) T cells: Foot soldiers of the immune system. *Immunity* 35:161–168.
3. Yoon H, Kim TS, Braciale TJ (2010) The cell cycle time of $CD8^+$ T cells responding in vivo is controlled by the type of antigenic stimulus. *PLoS One* 5:e15423.
4. O'Sullivan D, Pearce EL (2015) Targeting T cell metabolism for therapy. *Trends Immunol* 36:71–80.
5. Johnson TS, et al. (2014) Etoposide selectively ablates activated T cells to control the immunoregulatory disorder hemophagocytic lymphohistiocytosis. *J Immunol* 192: 84–91.
6. McNally JP, et al. (2014) Eliminating encephalitogenic T cells without undermining protective immunity. *J Immunol* 192:73–83.
7. O'Donnell M, Langston L, Stillman B (2013) Principles and concepts of DNA replication in bacteria, archaea, and eukarya. *Cold Spring Harb Perspect Biol* 5:a010108.
8. Zeman MK, Cimprich KA (2014) Causes and consequences of replication stress. *Nat Cell Biol* 16:2–9.
9. Brown EJ, Baltimore D (2000) ATR disruption leads to chromosomal fragmentation and early embryonic lethality. *Genes Dev* 14:397–402.
10. de Klein A, et al. (2000) Targeted disruption of the cell-cycle checkpoint gene ATR leads to early embryonic lethality in mice. *Curr Biol* 10:479–482.
11. Jeon Y, et al. (2011) TopBP1 deficiency causes an early embryonic lethality and induces cellular senescence in primary cells. *J Biol Chem* 286:5414–5422.
12. Murga M, et al. (2009) A mouse model of ATR-Seckel shows embryonic replicative stress and accelerated aging. *Nat Genet* 41:891–898.
13. Wang Y, et al. (2005) Mutation in Rpa1 results in defective DNA double-strand break repair, chromosomal instability and cancer in mice. *Nat Genet* 37:750–755.
14. Borowski A, et al. (2006) Structure and function of ETAA16: A novel cell surface antigen in Ewing's tumours. *Cancer Immunol Immunother* 55:363–374.
15. Wu C, et al. (2009) BioGPS: An extensible and customizable portal for querying and organizing gene annotation resources. *Genome Biol* 10:R130.
16. Miosge LA, et al. (2015) Comparison of predicted and actual consequences of missense mutations. *Proc Natl Acad Sci USA* 112:E5189–E5198.
17. Andrews TD, et al. (2012) Massively parallel sequencing of the mouse exome to accurately identify rare, induced mutations: An immediate source for thousands of new mouse models. *Open Biol* 2:120061.
18. Bass TE, et al. (2016) ETAA1 acts at stalled replication forks to maintain genome integrity. *Nat Cell Biol* 18:1185–1195.
19. Feng S, et al. (2016) Ewing tumor-associated antigen 1 interacts with replication protein A to promote restart of stalled replication forks. *J Biol Chem* 291: 21956–21962.
20. Haahr P, et al. (2016) Activation of the ATR kinase by the RPA-binding protein ETAA1. *Nat Cell Biol* 18:1196–1207.
21. Lee YC, Zhou Q, Chen J, Yuan J (2016) RPA-binding protein ETAA1 is an ATR activator involved in DNA replication stress response. *Curr Biol* 26:3257–3268.
22. Joshi NS, et al. (2007) Inflammation directs memory precursor and short-lived effector CD8(+) T cell fates via the graded expression of T-bet transcription factor. *Immunity* 27:281–295.
23. Sarkar S, et al. (2008) Functional and genomic profiling of effector CD8 T cell subsets with distinct memory fates. *J Exp Med* 205:625–640.
24. Russell TA, Stefanovic T, Tscharke DC (2015) Engineering herpes simplex viruses by infection-transfection methods including recombination site targeting by CRISPR/Cas9 nucleases. *J Virol Methods* 213:18–25.
25. van Lint A, et al. (2004) Herpes simplex virus-specific $CD8^+$ T cells can clear established lytic infections from skin and nerves and can partially limit the early spread of virus after cutaneous inoculation. *J Immunol* 172:392–397.
26. Simmons A, Tscharke DC (1992) Anti-CD8 impairs clearance of herpes simplex virus from the nervous system: Implications for the fate of virally infected neurons. *J Exp Med* 175:1337–1344.
27. Marshall HD, et al. (2011) Differential expression of Ly6C and T-bet distinguish effector and memory Th1 CD4(+) cell properties during viral infection. *Immunity* 35: 633–646.
28. Robinson MD, McCarthy DJ, Smyth GK (2010) edgeR: A Bioconductor package for differential expression analysis of digital gene expression data. *Bioinformatics* 26: 139–140.
29. Subramanian A, et al. (2005) Gene set enrichment analysis: A knowledge-based approach for interpreting genome-wide expression profiles. *Proc Natl Acad Sci USA* 102: 15545–15550.
30. Reimand J, Kull M, Peterson H, Hansen J, Vilo J (2007) g:Profiler: A web-based toolset for functional profiling of gene lists from large-scale experiments. *Nucleic Acids Res* 35:W193–200.
31. Heng TS, Painter MW; Immunological Genome Project Consortium (2008) The Immunological Genome Project: Networks of gene expression in immune cells. *Nat Immunol* 9:1091–1094.
32. Kumagai A, Lee J, Yoo HY, Dunphy WG (2006) TopBP1 activates the ATR-ATRIP complex. *Cell* 124:943–955.
33. Zhou ZW, et al. (2013) An essential function for the ATR-activation domain (AAD) of TopBP1 in mouse development and cellular senescence. *PLoS Genet* 9:e1003702.
34. Ruzankina Y, et al. (2007) Deletion of the developmentally essential gene ATR in adult mice leads to age-related phenotypes and stem cell loss. *Cell Stem Cell* 1: 113–126.
35. Kim J, et al. (2014) TopBP1 deficiency impairs V(D)J recombination during lymphocyte development. *EMBO J* 33:217–228.
36. O'Farrell PH, Stumpff J, Su TT (2004) Embryonic cleavage cycles: How is a mouse like a fly? *Curr Biol* 14:R35–R45.
37. Childs EJ, et al. (2015) Common variation at 2p13.3, 3q29, 7p13 and 17q25.1 associated with susceptibility to pancreatic cancer. *Nat Genet* 47:911–916.
38. Pircher H, Bürki K, Lang R, Hengartner H, Zinkernagel RM (1989) Tolerance induction in double-specific T-cell receptor transgenic mice varies with antigen. *Nature* 342: 559–561.
39. Ahmed R, Salmi A, Butler LD, Chiller JM, Oldstone MB (1984) Selection of genetic variants of lymphocytic choriomeningitis virus in spleens of persistently infected mice: Role in suppression of cytotoxic T lymphocyte response and viral persistence. *J Exp Med* 160:521–540.
40. Randall KL, et al. (2009) Dock8 mutations cripple B cell immunological synapses, germinal centers and long-lived antibody production. *Nat Immunol* 10:1283–1291.
41. McNamara HA, et al. (2017) Up-regulation of LFA-1 allows liver-resident memory T cells to patrol and remain in the hepatic sinusoids. *Sci Immunol* 2:eaaj1996.
42. Johnston RJ, et al. (2009) Bcl6 and Blimp-1 are reciprocal and antagonistic regulators of T follicular helper cell differentiation. *Science* 325:1006–1010.
43. Zajac AJ, et al. (1998) Viral immune evasion due to persistence of activated T cells without effector function. *J Exp Med* 188:2205–2213.
44. Quah BJ, Parish CR (2012) New and improved methods for measuring lymphocyte proliferation in vitro and in vivo using CFSE-like fluorescent dyes. *J Immunol Methods* 379:1–14.
45. Kim D, Langmead B, Salzberg SL (2015) HISAT: A fast spliced aligner with low memory requirements. *Nat Methods* 12:357–360.
46. Liao Y, Smyth GK, Shi W (2014) featureCounts: An efficient general purpose program for assigning sequence reads to genomic features. *Bioinformatics* 30:923–930.

Supporting Information

Miosge et al. 10.1073/pnas.1705795114

Table S1. Genes differentially expressed in *Etaa1*$^{\Delta Ex2/\Delta Ex2}$ vs. *Etaa1*$^{+/+}$ P14 cells at day 5 postinfection

logFC	logCPM	*P* value	FDR	MGI symbol
5.50	0.32	3.19E-41	6.62E-38	*Zfp750*
5.26	0.98	2.68E-48	8.33E-45	*Tnfsf4*
4.15	1.28	1.08E-43	2.51E-40	*Plk2*
4.08	0.40	6.45E-30	7.07E-27	*Ak1*
4.07	2.66	7.23E-108	6.74E-104	*Phlda3*
3.81	1.64	1.45E-09	1.80E-07	*Hspa1b*
3.69	4.84	0.00E+00	0.00E+00	*Serpine2*
3.41	1.07	3.06E-34	4.07E-31	*Zak*
3.21	1.24	3.23E-11	5.73E-09	*Tcrg-C4*
2.61	0.92	4.28E-08	3.51E-06	*Trgv2*
2.46	1.12	7.63E-16	2.79E-13	*Trim66*
2.33	1.59	3.04E-14	9.28E-12	*Batf3*
2.32	0.52	1.60E-07	1.14E-05	*Tcrg-C1*
2.28	0.33	2.86E-09	3.42E-07	*Eng*
2.25	2.75	3.11E-40	5.80E-37	*Fam212b*
2.25	2.81	3.60E-32	4.20E-29	*Bbc3*
2.19	0.44	2.75E-05	1.00E-03	*Capn11*
2.19	2.82	5.67E-08	4.46E-06	*Tcrg-C2*
2.11	2.79	2.16E-07	1.47E-05	*Fos*
2.00	2.28	9.31E-09	9.39E-07	*Xcl1*
2.00	0.11	3.74E-12	7.58E-10	*Ahnak2*
1.93	0.22	1.19E-11	2.21E-09	*Prrg4*
1.90	1.91	1.74E-20	1.08E-17	*Tnfsf8*
1.88	0.80	1.42E-05	5.78E-04	*Trbv29*
1.85	1.40	4.78E-15	1.59E-12	*Nos1*
1.85	5.99	5.13E-59	2.39E-55	*Cdkn1a*
1.85	3.40	4.10E-14	1.17E-11	*Jun*
1.79	0.79	3.11E-10	4.36E-08	*D630045J12Rik*
1.77	2.67	3.30E-32	4.10E-29	*Zfp365*
1.75	1.86	9.20E-17	3.83E-14	*Cd81*
1.72	3.35	5.15E-13	1.20E-10	*Lrp1*
1.71	4.25	1.51E-38	2.16E-35	*9030617O03Rik*
1.71	0.93	1.74E-10	2.61E-08	*Zfp385a*
1.68	1.76	2.61E-10	3.80E-08	*Fosb*
1.67	0.09	2.42E-05	9.05E-04	*mt-Tc*
1.63	0.71	5.03E-05	1.64E-03	*Trbv1*
1.61	3.95	4.61E-47	1.23E-43	*Psrc1*
1.56	0.94	2.67E-07	1.77E-05	*5830418P13Rik*
1.54	0.67	5.91E-09	6.45E-07	*Sdc1*
1.52	0.69	3.78E-03	4.68E-02	*Trbv13-1*
1.52	3.06	9.23E-25	8.19E-22	*Maats1*
1.49	0.76	1.17E-07	8.64E-06	*Mcam*
1.48	0.42	8.76E-06	3.77E-04	*Mx2*
1.47	0.69	6.37E-06	2.87E-04	*Gm10382*
1.47	1.98	1.06E-11	2.02E-09	*Dclk1*
1.44	1.64	1.15E-12	2.46E-10	*Ephx1*
1.42	2.98	3.92E-08	3.29E-06	*Tnfrsf10b*
1.41	0.73	1.00E-06	5.82E-05	*Cox6b2*
1.40	7.66	6.80E-05	2.06E-03	*Gm43549*
1.39	3.59	9.24E-17	3.83E-14	*Rgs16*
1.37	1.44	1.20E-05	4.98E-04	*Egr2*
1.37	7.59	3.78E-104	2.35E-100	*Ccng1*
1.36	3.26	7.21E-16	2.69E-13	*Cd80*
1.35	2.57	1.59E-16	6.18E-14	*Perp*

Table S1. Cont.

logFC	logCPM	*P* value	FDR	MGI symbol
1.34	0.48	6.43E-05	1.97E-03	*Bmpr1a*
1.33	0.94	1.20E-03	2.05E-02	*Trbv16*
1.32	4.43	1.04E-05	4.37E-04	*Ccl3*
1.30	2.40	3.95E-12	7.84E-10	*Tnfrsf4*
1.29	1.34	3.06E-07	2.00E-05	*Utf1*
1.28	0.55	2.37E-04	5.77E-03	*Trbv20*
1.26	4.81	2.45E-49	9.16E-46	*Zmat3*
1.25	2.12	4.06E-14	1.17E-11	*Dcxr*
1.25	0.32	5.08E-05	1.66E-03	*Gm9522*
1.23	3.46	8.46E-23	6.57E-20	*Snhg15*
1.23	0.41	3.70E-06	1.80E-04	*Ogdhl*
1.23	1.80	5.88E-04	1.16E-02	*Trbv13-2*
1.17	0.02	1.50E-04	4.02E-03	*Spint1*
1.16	0.01	2.30E-03	3.26E-02	*Bst1*
1.16	0.47	1.75E-05	6.89E-04	*Etv4*
1.16	4.45	1.10E-04	3.11E-03	*Ccl4*
1.15	0.36	1.14E-03	1.98E-02	*Tctex1d2*
1.15	0.62	3.16E-05	1.11E-03	*Slc4a11*
1.14	1.24	7.19E-06	3.19E-04	*Irak1bp1*
1.13	1.39	3.35E-08	2.86E-06	*Map7*
1.13	0.11	1.70E-03	2.60E-02	*Hectd2*
1.13	3.57	4.36E-20	2.62E-17	*Slc19a2*
1.10	0.32	4.87E-04	9.95E-03	*Rasal2*
1.10	4.33	1.52E-12	3.18E-10	*Tnfrsf8*
1.08	1.98	7.46E-07	4.49E-05	*Filip1*
1.07	3.06	4.07E-11	7.03E-09	*Nebl*
1.07	5.71	2.17E-24	1.84E-21	*Mx1*
1.07	1.08	6.94E-04	1.32E-02	*Siglec1*
1.07	0.58	5.86E-05	1.84E-03	*Gm10451*
1.06	0.07	2.60E-04	6.22E-03	*Cdc42bpb*
1.05	0.24	1.53E-03	2.44E-02	*Snord83b*
1.05	5.59	9.62E-16	3.45E-13	*Trp53inp1*
1.04	1.29	4.85E-06	2.25E-04	*S100a3*
1.04	1.47	2.35E-06	1.25E-04	*Cd200*
1.04	5.27	4.77E-05	1.57E-03	*Ifng*
1.04	1.43	3.56E-03	4.47E-02	*Egr3*
1.04	1.89	2.24E-06	1.19E-04	*Slc29a2*
1.03	3.82	3.94E-06	1.90E-04	*Nr4a3*
1.03	0.88	3.47E-04	7.75E-03	*Acsl3*
1.01	3.17	1.70E-13	4.35E-11	*Plxna1*
−1.01	0.45	5.55E-04	1.11E-02	*Enho*
−1.02	4.20	4.89E-08	3.95E-06	*Tppp3*
−1.13	1.83	4.90E-08	3.95E-06	*Crybb1*
−1.24	0.33	1.74E-04	4.52E-03	*Gm4208*
−1.27	3.17	6.09E-13	1.35E-10	*Epha8*
−1.28	2.40	9.25E-11	1.51E-08	*Srcin1*
−1.31	0.41	7.65E-04	1.42E-02	*Gm37829*
−1.33	0.36	8.59E-07	5.07E-05	*Gm11611*
−1.34	0.14	4.47E-05	1.49E-03	*Rsph10b*
−1.41	2.35	1.49E-07	1.06E-05	*Ablim2*
−1.43	3.79	1.80E-21	1.20E-18	*S1pr5*
−1.57	0.05	3.62E-05	1.25E-03	*Gm38102*
−1.57	2.39	3.83E-09	4.38E-07	*Mir142hg*
−1.60	5.93	1.21E-21	8.71E-19	*Cx3cr1*
−2.70	0.79	1.31E-10	2.07E-08	*Plagl1*

Table S2. TF-binding motifs enriched in genes up-regulated within *Etaa1*$^{\Delta Ex2/\Delta Ex2}$ P14 cells

TF-binding motif	Motif ID	*P* value
Factor: p53; motif: RGRCWWGYCYNGRCWWGYYY; match class: 0	TF:M01652_0	1.85E-08
Factor: p53; motif: RGRCWWGYCYNGRCWWGYYY; match class: 1	TF:M01652_1	4.95E-08
Factor: p53; motif: GGACATGCCCGGGCATGTCY; match class: 0	TF:M00034_0	0.00000104
Factor: P53; motif: RGRCATGYCYRGRCATGYYY; match class: 1	TF:M01651_1	0.00000604
Factor: P53; motif: RGRCATGYCYRGRCATGYYY; match class: 0	TF:M01651_0	0.00000619
Factor: p53; motif: GGACATGCCCGGGCATGTCY; match class: 1	TF:M00034_1	0.00000952
Factor: P53; motif: NNNNNACAWGCCYNNN; match class: 0	TF:M07054_0	0.00000999
Factor: BCL6B; motif: NNNNCCGCCCCWNNNN; match class: 1	TF:M02844_1	0.00493
Factor: P53; motif: NNNNNACAWGCCYNNN; match class: 1	TF:M07054_1	0.00993
Factor: BTEB2; motif: RGGGNGKGGN; match class: 1	TF:M07277_1	0.0131
Factor: AHR; motif: CACGCN; match class: 1	TF:M01855_1	0.0197
Factor: BEN; motif: CAGCGRNV; match class: 1	TF:M01240_1	0.0225
Factor: AP-4; motif: RNCAGCTGC; match class: 0	TF:M00927_0	0.0256
Factor: HTF4; motif: RACAGCTGNNN; match class: 0	TF:M07134_0	0.0303

Other Supporting Information Files

SI Appendix (PDF)

APPENDIX 1. Full histopathology report from three *Etaa1*$^{+/+}$ and three *Etaa1*$^{\Delta Ex2/\Delta Ex2}$ female mice (62 weeks of age)

Contacts:
Tina Cardamone, Manager APN (Melbourne)
Louise Pontell, Research Histologist
Professor Janet Keast, Head APN (Melbourne)

Australian Phenomics Network
Histopathology and Organ Pathology
The University of Melbourne
Department of Anatomy and Neuroscience
Grattan Street, PARKVILLE, VIC 3010
T: +61 3 83448044 F: +61 3 93479619
apn-info@unimelb.edu.au

9.1 Histopathology Report

Case Number	APN16/042 The John Curtin School of Medical Research, The Australian National University (Lisa Miosge)
Registration Date	Tue 06/12/2016
Animal Details	ENU28 11 G7#338, WT DOB: 29/09/15 & 02/10/15, 62 weeks, Female, 27.5g, Black Strain: C57Bl/6 Ncrl ENU28 11 G7#340, WT DOB: 29/09/15 & 02/10/15, 62 weeks, Female, 30.8g, Black Strain: C57Bl/6 Ncrl ENU28 11 G7#345, WT DOB: 29/09/15 & 02/10/15, 62 weeks, Female, 36.0g, Black Strain: C57Bl/6 Ncrl ENU28 11 G7#355, Homozygous DOB: 29/09/15 & 02/10/15, 62 weeks, Female, 26.9g, Black Strain: C57Bl/6 Ncrl ENU28 11 G7#359, Homozygous DOB: 29/09/15 & 02/10/15, 62 weeks, Female, 27.0g, Black Strain: C57Bl/6 Ncrl ENU28 11 G7#360, Homozygous DOB: 29/09/15 & 02/10/15, 62 weeks, Female, 19.8g, Black Strain: C57Bl/6 Ncrl
DoD / Necropsy	Wed 07/12/2016
Death	CO2
Origin	The John Curtin School of Medical Research, The Australian National University
Treatment	ENU ENU induced mutation in a gene suspected to be involved in DNA repair (L. Miosge).
Species / Breed / Strain	
Animal Health Facility	Australian Phenomics Facility, ANU POSITIVE for Staphylococcus aureus POSITIVE for Entamoeba muris POSITIVE for Tritrichomonas muris POSITIVE for Pasteurellaceae spp (not including pneumotropica) POSITIVE for Pasteurella pneumotropica POSITIVE for Helicobacter spp POSITIVE for Mouse Norovirus POSITIVE for Chilomastix bettencourti

Organs Examined	Adrenal glands, Bladder, Bone marrow, Brain, Cecum, Cervix, Clitoral gland, Colon, Duodenum, Eyes, Gall bladder, Harderian glands, Head, Heart, Hind leg (Long bone, Bone marrow, Synovial joint, Skeletal muscle), Ileum, Jejunum, Kidney, Liver, Lungs, Mammary tissue, Mesenteric lymph node, Other tissue, Ovaries, Oviducts, Pancreas, Salivary glands and Regional lymph nodes, Skin, Spinal cord, Spleen, Stomach, Tail, Thymus, Thyroids, Trachea, Uterus, Vagina
Macroscopic Observations	Date of transport to the APN: Wednesday 7th December Time animal/tissue dispatched: 2:30pm Tuesday 6th December Courier/Transportation details: Jetpets At the time of necropsy, the animals appeared well nourished, well groomed, active/curious and healthy with normal movement and gait. There were no observable dermal lesions and no nasal/ocular discharges. Animal #340 showed excessive abdominal fat around the reproductive organs as well as a pale tan lesion running along the ascending portion of its colon measuring 25x10x5mm. #338 also showed some excessive fat around the reproductive organs and #359 had an enlarged spleen. The gastrointestinal tracts of the remaining animals contained ample ingesta and the thoracic and abdominal viscera showed no macroscopic abnormalities.

Microscopic Observations

Blood Report:
Most most readings were within the normal mouse reference intervals.
The platelet count for ENU28 11 G7#355 & ENU28 11 G7#360 was low, but as the MPV was within range, this is likely to not be significant. Decreased platelets are common haematologic finding in mice. However this change is often secondary to blood collection difficulties rather than a true decrease in platelet counts. Mouse platelets readily aggregate and instrument generated platelet counts will underestimate true platelet counts in the presence of platelet clumping.
The eosinophil count for all animals was elevated, this is a common occurrence in mice.

The following micromorphological changes observed in the knock-outs were also observed in the control animals #338, #340 and #345.
Ceroid-lipofuscin laden cells in the ovaries: #338, #340 and #345
Cystic oviducts: #338, #340 and #345
Cystic endometrial hyperplasia of the uterus: #340 and #345
Inflammatory aggregates within the urinary bladder: #338 and #345
Inflammatory infiltrates within the liver: #340
Inflammatory infiltrates within various organs (including pancreas, kidneys, salivary glands, lungs and Harderian glands): #338, #340 and #345
Basophilic valvular changes in the heart: #340 and #345
Reduction in density of spiral ganglion cells: #340

Note:
(i) Reactive lymph nodes are defined as mild follicular hyperplasia, germinal centre formation and occasional sinus histiocytosis - a common finding in mice
(ii) Mild extramedullary hematopoiesis (EMH) identified in the red pulp of all the spleens, a common finding in the mouse. EMH consists of erythroid precursors, myeloid precursors, megakaryocytes or all three. While some degree of extramedullary hematopoiesis is present in normal rodents, especially in mice, increased extramedullary hematopoiesis can result from hematotoxic insult, systemic anemia, and infections elsewhere in the body. A.W Suttie, 2006
(iii) Focal inflammatory cell aggregates consisting of mononuclear, polymorphonuclear, and/or histiocytic cells are frequently observed in ageing mice (R. R. Maranport). These can be present as lymphoid aggregates found in various tissues including the renal pelvis, bladder, lungs, liver (C. Pettan-Brewer and P. M. Treuting "Practical pathology of aging mice") and salivary glands (M. R. Anver and D.C. Haines " the

Laboratory Mouse").
(iv) Intracellular eosinophilic crystals may occasionally be seen in the lungs of mice. It has been reported that these structures may represent eosinophil granules at various stages of degradation (Murray and Luz, 1990). Others believe the crystals may represent haemoglobin breakdown following uptake by macrophages (Shultz et al., 1984).

Summary KO animals:

#355
Ovaries: ceroid-lipofuscin laden cells (58992, 59365)
Oviducts: Query - appear cystic (58992, 59365)
Uterus: cystic endometrial hyperplasia (58992, 59365)
Urinary bladder: inflammatory aggregate (59365)
Liver: inflammatory infiltrates (58990)
Kidneys: inflammation, tubular degeneration protein casts. Query: loss of typical nodal architecture of renal lymph nodes (58991, 59367)
Salivary glands: inflammatory infiltrates (58987). Query: one lymph node displays a loss of typical reactive architecture (59366)
Lungs: inflammatory infiltrates (58996, 59368)
Heart: basophilic valvular changes (58985)

#359
Mammary glands: inflammatory aggregate (58963)
Ovaries: ceroid-lipofuscin laden cells (58964, 59371, 59372)
Oviducts: Query - appear cystic (58964, 59371, 59372)
Uterus: cystic endometrial hyperplasia (58964, 59371, 59372), inflammatory infiltrates (59371)
Liver: inflammatory infiltrates (58962)
Stomach: inflammatory infiltrates (58968)
Kidneys: inflammatory infiltrates and protein casts (58953, 59369)
Salivary glands: inflammatory infiltrates and lipofucsin laden cells (58965, 59370)
Lungs: inflammatory infiltrates and eosinophilic crystals (58966)
Thymus: cyst-like structure (58967)
Heart: basophilic valvular changes (58950)
Harderian glands: inflammatory aggregate (58957)

#360
Ovaries: ceroid-lipofuscin laden cells (59374, 59375)
Oviducts: Query - appears cystic (59374, 59375)
Uterus: cystic endometrial hyperplasia (58929, 59374, 59375)
Vagina: inflammatory infiltrates (59375)
Urinary bladder: inflammatory aggregate (59374)
Liver: inflammatory infiltrates (58934)
Pancreas: inflammatory infiltrates (58924, 58940)
Kidneys: inflammatory infiltrates and protein casts (58935, 59373)
Salivary glands: inflammatory infiltrates (58926)
Lungs: inflammatory infiltrates (58931)
Heart: Query - degenerating myocytes (58938)
Harderian gland: inflammatory aggregate (58939)

Summary WT animals:

#338
Ovaries: ceroid-lipofuscin laden cells (59063, 59358)
Oviducts: Query - appears cystic (59063, 59358)
Urinary Bladder: inflammatory aggregates (59063, 59358)
Pancreas: inflammatory infiltrates (59071, 59075)
Kidneys: inflammatory infiltrates and protein casts (59066, 59360)
Salivary glands: inflammatory infiltrates (59062, 59359)
Lungs: inflammatory infiltrates (59081)
Heart: basophilic valvular changes (59069)
Skin: inflammatory infiltrates (59076)
Harderian gland: inflammatory infiltrates (59070)

#340
Mammary glands: inflammation (59038)
Ovaries: ceroid-lipofuscin laden cells (59039, 59361)
Oviducts: Query - appears cystic (59039, 59361)
Uterus: cystic endometrial hyperplasia (59039, 59361)
Liver: inflammatory infiltrates (59036, 59037)
Colon: lymphoid lesion (59051)
Pancreas: inflammatory infiltrates (59042, 59045)
Kindeys: protein cast (59036)
Salivary glands: inflammatory infiltrates (59040)
Lungs: inflammation and haemorrhage (59047, 59362)
Heart: basophilic valvular changes (59052)
Head: reduction in density of spiral ganglion cells (59058)

#345
Ovaries: ceroid-lipofuscin laden cells (59025, 59363)
Oviducts: Query - appears cystic? (59025, 59363)
Uterus: cystic endometrial hyperplasia (59025, 59363)
Urinary bladder: inflammatory aggregate (59363)
Pancreas: inflammatory infiltrates (59006, 59017, 59022)
Kidneys: inflammatory infiltrates (59364)
Salivary glands: inflammatory infiltrates and query: loss of typical nodal architecture (59024).
Lungs: inflammatory infiltrates (59010)
Heart: basophilic valvular changes (59015)
Harderian glands: inflammatory infiltrates (59016)

ENU28 11 G7#338 (control)

Macro Observations

Spleen: 14x4x2mm,
Kidneys: 12x7x6mm, symmetrical
Thymus: 9x6x2mm
Heart: 9x6x5mm
Brain: 14x10x5mm, symmetrical
Pituitary gland identified, macroscopically normal
Tail 82mm (straight)
Teeth, tongue and oral mucosa unremarkable - Head harvested for evaluation of auditory and vestibular structures
Tail suspension test for neurological defects-negative

Excessive fat (+) around reproductive organs

Micro Observations

Marrow smear: Examination of the smear showed representative cells from the myeloid and erythroid series. Conspicuous cells from the lymphoid series. Numerous and unremarkable megakaryoblasts.
(59089)

Peripheral blood smear: Examination of the smear showed red blood cells (majority of cells shown), occasional white blood cells including lymphocytes, segmented neutrophils, platelets (clumps) and monocytes. No discernible morphological changes or detectable parasites.
(59088)

Ovaries: Moderate interstitial age related ceroid-lipofuscin laden cells (59063, 59358)

Oviducts: Query - portions of serosa appear mildly cystic (59063, 59358)
Pathology to comment

Urinary Bladder: Moderate multifocal submucosal lymphocytic aggregates (59063, 59358)

Pancreas: Mild multifocal perivascular lymphocytic infiltrates (59071, 59075)

Kidneys: In both kidneys - mild multifocal perivascular lymphocytic infiltrates mainly adjacent or near renal cavity. Several protein casts within medulla and papilla (59066, 59360)

Salivary glands: Mild to moderate multifocal perivascular lymphocytic infiltrates within the submandibular and sublingual glands (59062, 59359)

Lungs: Mild focal perivascular lymphocytic infiltrates (59081)

Heart: Mild basophilic valvular changes, likely to be age related (59069)

Skin: Mild focal lymphocytic infiltrates within the subcutis (59076)

Harderian gland: Mild focal perivascular lymphocytic infiltrates (59070)

ENU28 11 G7#340 (control)

Macro Observations

Spleen: 20x8x2mm
Kidneys: 10x6x5mm, symmetrical
Thymus: 7x7x2mm
Heart: 10x6x5mm
Brain: 15x10x5mm, symmetrical
Pituitary gland identified, macroscopically normal
Tail 85mm (straight)
Teeth, tongue and oral mucosa unremarkable - Head harvested for evaluation of auditory and vestibular structures
Tail suspension test for neurological defects-negative

Excessive fat (+++) around reproductive organs.
Pale tan lesion 25x10x5mm running along the ascending colon.

Micro Observations

Marrow smear: Examination of the smear showed representative cells from the myeloid and erythroid series. Conspicuous cells from the lymphoid series. Numerous and unremarkable megakaryoblasts.
(59061)

Peripheral blood smear: Examination of the smear showed red blood cells (majority of cells shown), occasional white blood cells including lymphocytes, segmented neutrophils, platelets (clumps) and monocytes. No discernible morphological changes or detectable parasites.
(59060)

Mammary glands: Mild focal lymphocytic aggregate adjacent to a subcutical nerve fascicle (59038)

Ovaries: Moderate to severe interstitial age related ceroid-lipofuscin laden cells (59039, 59361)

Oviducts: Query - portions of serosa appear mildly cystic (59039, 59361)

Uterus: Mild cystic endometrial hyperplasia, a common age related lesion (59039, 59361)

Liver: Moderate multifocal perivascular lymphocytic infiltrates (59037)

Colon: Well circumscribed large lymphoid lesion consisting of large polymorphhic lymphoid cells that are non impinging on the colon (59051)
Pathology to comment

Pancreas: Mild multifocal perivascular lymphocytic infiltrates (59042, 59045)

Kindey: Single short protein cast within medulla (59036)

Salivary glands: Mild multifocal perivascular lymphocytic infiltrates within the submandibular and sublingual glands (59040)

Lungs: Moderate multifocal perivascular inflammation, moderate multifocal haemorrhage and some areas of varying degrees of congestion and atelectasis (59047, 59362)
Pathology to comment

Heart: Mild basophilic valvular changes, likely to be age related (59052).

Head: Reduction in density of the spiral ganglion cells, a common age related feature (59058)

ENU28 11 G7#345 (control)

Macro Observations

Spleen: 16x4x3mm
Kidneys: 10x6x5mm, symmetrical
Thymus: 10x5x2mm
Heart: 8x5x5mm
Brain: 13x10x6mm, symmetrical
Pituitary gland identified, macroscopically normal
Tail 80mm (straight)
Teeth, tongue and oral mucosa unremarkable - Head harvested for evaluation of auditory and vestibular structures
Tail suspension test for neurological defects-negative

Micro Observations

Marrow smear: Examination of the smear showed representative cells from the myeloid and erythroid series. Conspicuous cells from the lymphoid series. Numerous and unremarkable megakaryoblasts.
(59032)

Peripheral blood smear: Examination of the smear showed red blood cells (majority of cells shown), occasional white blood cells including lymphocytes, segmented neutrophils, platelets (clumps) and monocytes. No discernible morphological changes or detectable parasites.
(59033)

Ovaries: Mild to moderate interstitial age related ceroid-lipofuscin laden cells (59025, 59363)

Oviducts: Query - portions of serosa appear mildly cystic (59025, 59363)

Uterus: Mild cystic endometrial hyperplasia, a common age related lesion (59025, 59363)

Urinary bladder: Mild focal submucosal lymphocytic aggregate (59363)

Pancreas: Mild multifocal perivascular lymphocytic infiltrates (59006, 59017, 59022)

Kidney: Mild focal perivascular lymphocytic infiltrates (59364)

Salivary glands: Mild to moderate perivascular lymphocytic infiltrates. Query - loss of typical nodal architecture of the regional lymph nodes (59024)
Pathology to comment

Lung: Mild focal perivascular/peribronchial lymphocytic infiltrates (59010)

Heart: Mild basophilic valvular changes, likely to be age related (59015)

Harderian glands: Mild multifocal perivascular lymphocytic infiltrates (59016)

ENU28 11 G7#355

Macro Observations

Spleen: 15x4x2mm
Kidneys: 12x5x5mm, symmetrical
Thymus: 6x5x2mm
Heart: 10x6x5mm
Brain: 14x10x5mm, symmetrical
Pituitary gland identified, macroscopically normal
Tail 80mm (straight)
Teeth, tongue and oral mucosa unremarkable - Head harvested for evaluation of auditory and vestibular structures
Tail suspension test for neurological defects-negative

Micro Observations

Marrow smear: Examination of the smear showed representative cells from the myeloid and erythroid series. Conspicuous cells from the lymphoid series. Occassional and unremarkable megakaryoblasts.
(59004)

Peripheral blood smear: Examination of the smear showed red blood cells (majority of cells shown), occasional white blood cells including lymphocytes, segmented neutrophils, platelets (clumps) and monocytes. No discernible morphological changes or detectable parasites.
(59005)

Mammary glands

Section shows typical mammary fat pad with developing lactiferous ducts, blood vessels and nerve bundles. Some scattered mast cells identified; a common finding in mouse mammary tissue.
(58993)
No lesions of significance

Ovaries/Oviducts

Section shows ovaries containing follicles at various stages of development (primary through to antral), several corpora lutea and mild to moderate interstitial age related ceroid-lipofuscin laden cells.
Unremarkable oviduct micromorphology with typical columnar epithelium and mucosal folds.
Query - portions of serosa appear mildy cystic.
(58992, 59365)

Comments:

Pathology to comment

Uterus/Cervix/Vagina/Clitoral gland

The architecture of the endometrium/endometrial glands, myometrium and adventitia are discernible.
Sections show mild cystic endometrial hyperplasia, a common age related lesion.
Some neutrophils and low numbers of lymphocytes identified in the endometrial glands; a common finding within a non-inflamed endometrium during the phases of estrus.
The micromorphology of the uterus and vagina places the animal at metestrus.
(58992, 59365)

Urinary Bladder

Distended bladder with discernible urothelium and detrusor muscle.
Sections show a mild focal perivascular lymphocytic aggregate within the submucosa (59365).
Sections also include unremarkable ureter and urethra.
(58992, 59365)

Liver/Gall bladder

Section shows liver parenchyma including hepatocytes, Kupffer cells, portal triads and central veins.
Section also shows mild focal perivascular and parenchymal lymphocytic aggregate.
Unremarkable Gall bladder.
(58990)

Comments:

Pathology to comment

Stomach

Section shows unremarkable fore and glandular portions of the stomach with limiting ridge.
Section also includes pylorus sphincter and duodenal bulb.
(58994)
No lesions of significance

Small Intestine (Duodenum, Jejunum & Ileum)/GALT

Section shows typical mucosal villi and submucosal layers.
Peyer’s patches displayed typical reactive nodal histology.
(58979, 58983)
No lesions of significance

Cecum/Colon/GALT

Typical mucosal folds and submucosal layers and occasional lymphoid cluster (Peyer's patch)
(58978, 58981)
No lesions of significance

Mesenteric lymph node

Section does not include mesenteric lymph node.

Spleen

Mild follicular hyperplasia and germinal center formation in the white pulp.
Moderate extramedullary hematopoiesis and Hemosiderin laden macrophages identified in the red pulp, a common finding in the mouse.
(58989)
No lesions of significance

Pancreas

Section shows representative exocrine tissue (serous acini) and endocrine tissue (islets of Langerhans).
(58989)
No lesions of significance

Kidney

Section shows a cortex, medulla, and papilla. There is a uniform distribution of Glomeruli and accompanying nephron components.
Mild multifocal pervascular inflammation, mild multifocal tubular degeneration and a few dilated tubules within the cortex.
Scattered, and at times enlarged dilated protein casts identified mainly within the medulla and papilla.
Query: loss of typical nodal architecture of renal lymph nodes.
(58991, 59367)

Comments:

Pathology to comment

Adrenal glands

Section shows adrenal glands with typical cortex/medulla distribution.
A few age related lipofuscin laden cells at the cortical-medullary junction and mild subcapsular spindle cell hyperplasia, a common background lesion.
(59367)

Salivary glands and Regional lymph nodes

Section shows submandibular gland with mild focal perivascular inflammation and unremarkable sublingual and parotid glands (58987).
The regional lymph nodes displayed mild follicular hyperplasia with germinal centre formation, indicating a reactive state.
Query: one lymph node displays a loss of typical reactive nodal architecture (59366).
(58987, 59366)

Comments:

Pathology to comment

Thyroids

Normal lateral lobes of the thyroid gland with typical colloid secreting follicles lined by cuboidal epithelium.
(58996, 59368)
No lesions of significance

Trachea/Lungs

Section shows lung micromorphology demonstrating parenchyma/alveoli, bronchioles and blood vessels with mild to moderate multifocal pericasvular/peribrochial lymphocytic infiltrates .
Trachea with unremarkable mucosal epithelial lining and hyaline cartilage.
Oesophagus with typical features including stratified squamous epithelium.
(58996, 59368)

Comments:

Pathology to comment

Thymus

Section shows typical medulla/cortex distribution and micromorphology.
(58997)
No lesions of significance

Heart/chambers/vessels/valves

Typical micromorphology observed in cardiac muscle, chambers, valves and vessels of the heart.
The cardiac muscle fibres demonstrated typical features including central nuclei, branching fibres and striations.
Some mild basophilic valvular changes, likely to be age related.
(58985)

Comments:

Pathology to comment

Skin

Typical dermal appendages and distribution. Unremarkable thin layer of striated muscle (panniculus carnosus).
(58986)
No lesions of significance

Tail

Section shows typical tail components including keratinized squamous epithelium, dense regular connective tissue, tendons, caudal vertebra, bone marrow, intervertebral disc, skeletal muscle, nerves and blood vessels.
(58995)
No lesions of significance

Eyes/Harderian glands

Section shows eyes with unremarkable retina, cornea, iris, ciliary body, lens, sclera and choroid. Typical branched tubuloalveolar formation of the Harderian gland.
Section also includes portion of unremarkable optic nerve and extraocular muscles.
(58984)
No lesions of significance

Brain

Sections were prepared from the standard levels of the brain:

Level I forebrain: including cortex, corpus callosum, caudate putamen and lateral ventricles (Bregma 1.10mm)
Level II midbrain: including the hippocampus, thalamus, hypothalamus and lateral and third ventricles (Bregma -1.46mm)
Level III hindbrain: includes the cerebellum, pons and fourth ventricle (Bregma -5.52mm)

Sections of brain stained with Haematoxylin and Eosin, Luxol Fast Blue appear symmetrical with no ventricular dilation observed, unremarkable meninges and typical lamination.
The cerebellum appears symmetrical with typical architecture and Purkinje cells.
There was no evidence of neuronal loss and the myelination appeared normal.
(58980, 58998)
No lesions of significance

Comments:

Neuropatholoy to comment

Spinal cord

Representative thoracic and lumbar region of spinal cord, vertebral bone, striated muscle, peripheral nerves and bone marrow.
(58988)
No lesions of significance

Comments:

Neuropatholoy to comment

(Hind leg) Long bone/Bone marrow/Synovial joint/Skeletal muscle

Section shows unremarkable long bone, striated muscle, synovial joint and bone marrow including conspicuous megakaryoblasts. The skeletal muscle shows consistent fiber size with peripheral nuclei.
(58982)
No lesions of significance

Head

Multiple levels through the head demonstrate dermal appendages, nasal cavity, oral cavity, teeth and tongue including muscle bundles. Sections also show unremarkable pituitary gland including pars intermedia, pars distalis and pars nervosa as well and the trigeminal nerve/ganglia (58999). The outer and middle regions of the ear are discernible. The tympanic membrane is intact and the ossicles are unremarkable and include the stapedial annular ligaments (59000-59003). Typical components of the inner ear including bony labyrinth, organ of corti, stria vascularis and scala cavities are discernible. Based on multiple levels, the organ of corti is unremarkable with no discernible loss of inner/outer hair cells and typical tectorial membrane (59000-59003).

The cochlear nerve and spiral ganglion is also demonstrated and based on several levels, there is no reduction in the density of the spiral ganglion cells. Examples of otolith organs can be seen with typical features such as the hair cells and mineral otoliths. The ampulla including the crista ridge with hair cells is discernible (59000-59003).

No lesions of significance
(58999-59003)

ENU28 11 G7#359

Macro Observations

Spleen: 25x8x2mm, large
Kidneys: 12x7x6mm, symmetrical
Thymus: 7x7x2mm
Heart: 10x6x6mm
Brain: not measured, symmetrical
Pituitary gland identified, macroscopically normal
Tail 85mm (straight)
Teeth, tongue and oral mucosa unremarkable - Head harvested for evaluation of auditory and vestibular structures
Tail suspension test for neurological defects-negative

Micro Observations

Marrow smear: Examination of the smear showed representative cells from the myeloid and erythroid series. Conspicuous cells from the lymphoid series. Occassional and unremarkable megakaryoblasts.
(58977)

Peripheral blood smear: Examination of the smear showed red blood cells (majority of cells shown), occasional white blood cells including lymphocytes, segmented neutrophils, platelets (clumps) and monocytes. No discernible morphological changes or detectable parasites.
(58976)

Mammary glands

Section shows mammary fat pad with developing lactiferous ducts, blood vessels, nerve bundles and a lymph node with typical nodal histology.
Focal lymphocytic aggregate surrounding a single lactiferous duct.
Some scattered mast cells identified; a common finding in mouse mammary tissue.
(58963)

Ovaries/Oviducts

Section shows ovaries containing follicles at various stages of development (primary through to antral), several corpora lutea and mild interstitial age related ceroid-lipofuscin laden cells.
Unremarkable oviduct micromorphology with typical columnar epithelium and mucosal folds.
Query - portions of serosa appear mildy cystic.
(58964, 59371, 59372)

Comments:

Pathology to comment

Uterus/Cervix/Vagina/Clitoral gland

The architecture of the endometrium/endometrial glands, myometrium and adventitia are discernible.
Section shows mild cystic endometrial hyperplasia (58964, 59371, 59372), a common age related lesion, and mild focal lymphocytic perivascular infiltrates within the myometrium (59371).
Some neutrophils and low numbers of lymphocytes identified in the endometrial glands; a common finding within a non-inflamed endometrium during the phases of estrus.

The micromorphology of the uterus and vagina places the animal at estrus.
(58964, 59371, 59372)

Urinary Bladder

Unremarkable collapsed bladder with typical urothelium and detrusor muscle.
Section includes unremarkable urethra.
(58964, 59371, 59372)
No lesions of significance

Liver/Gall bladder

Section shows liver parenchyma including hepatocytes, Kupffer cells, portal triads and central veins with mild to moderate multifocal perivascular and parenchymal lymphocytic infiltrates.
Unremarkable Gall bladder.
(58962)

Comments:

Pathology to comment

Stomach

Section shows fore and glandular portions of the stomach with limiting ridge and mild focal lymphocytic aggregates within the submucosa.
Section also includes pylorus sphincter and duodenal bulb.
(58968)

Small Intestine (Duodenum, Jejunum & Ileum)/GALT

Section shows typical mucosal villi and submucosal layers and occasional lymphoid cluster (Peyer's patch)
(58952, 58956)
No lesions of significance

Cecum/Colon/GALT

Typical mucosal folds and submucosal layers and occasional lymphoid cluster (Peyer's patch).
Section includes pancreas with mild multifocal perivascular lymphocytic infiltrates (58955).
(58954, 58955).

Mesenteric lymph node

Section shows mesenteric lymph node with typical reactive micromorphology including mild follicular hyperplasia, germinal centre formation and mild sinus histiocytosis.
(58965, 59370)
No lesions of significance

Spleen

Mild follicular hyperplasia of the white pulp.
Mild extramedullary hematopoiesis and Hemosiderin laden macrophages identified in the red pulp of the spleen, a common finding in the mouse.
(58959)
No lesions of significance

Pancreas

Section shows representative exocrine tissue (serous acini) and endocrine tissue (islets of Langerhans).
There is mild multifocal perivascular lymphocytic infiltrates in one section of the spleen (58955).
(58955, 58956, 58959)

Kidney

Section shows a cortex, medulla, and papilla. There is a uniform distribution of Glomeruli with unremarkable micromorphology.
There are mild to moderate multifocal perivascular lymphocytic infiltrates (58953, 59369), a few scattered short casts and one enlarged protein cast within the medulla (59369).
Section also includes renal lymph nodes with typical reactive nodal histology and mild sinus histiocytosis.
(58953, 59369)

Comments:

Pathology to comment

Adrenal glands

Section shows adrenal glands with typical cortex/medulla micromorphology.
A few age related lipofuscin laden cells at the cortical-medullary junction and mild subcapsular spindle cell hyperplasia, a common background lesion
(58953, 59369)

Salivary glands and Regional lymph nodes

Section shows unremarkable submandibular, sublingual and parotid glands.
Nearby associated glands shows mild multifocal lymphocytic aggregates, mild diffuse neutrophilic infiltrates within the surrounding connective tissue and a few lipofucsin laden cells within the gland. Associated glands are surrounded by connective tissue and axillary mammary glands.
The regional lymph nodes displayed mild follicular hyperplasia with germinal centre formation, indicating a reactive state.
(58965, 59370)

Comments:

Pathology to comment

Thyroids

Unremarkable colloid secreting follicles identified. Section also shows a small sheet-like mass of polygonal cells, characteristic of the parathyroid gland.
(58966)
No lesions of significance

Trachea/Lungs

Section shows lung micromorphology demonstrating parenchyma/alveoli, bronchioles, blood vessels and parabronchial lymph node with mild to moderate multifocal perivascular lymphocytic infiltrates.
Focal intracellular eosinophilic crystals within the cytoplasm of alveolar macrophages.
Trachea with unremarkable mucosal epithelial lining and hyaline cartilage.
Oesophagus with typical features including stratified squamous epithelium.
(58966)

Comments:

Pathology to comment

Thymus

Section shows typical medulla/cortex distribution and micromorphology.
Within the cortex, medium sized cyst like structure containing macrophages and cellular debris.
(58967)

Comments:

Pathology to comment

Heart/chambers/vessels/valves

Typical micromorphology observed in cardiac muscle, chambers and vessels of the heart.
The cardiac muscle fibres demonstrated typical features including central nuclei, branching fibres and striations.
Some mild basophilic valvular changes, likely to be age related.
(58950)

Comments:

Pathology to comment

Skin

Typical dermal appendages and distribution. Unremarkable thin layer of striated muscle (panniculus carnosus).
(58958)
No lesions of significance

Tail

Section shows typical tail components including keratinized squamous epithelium, dense regular connective tissue, tendons, caudal vertebra, bone marrow, intervertebral disc, skeletal muscle, nerves and blood vessels.
(58961)
No lesions of significance

Eyes/Harderian glands

Section shows eyes with unremarkable retina, cornea, iris, ciliary body, lens, sclera and choroid.
Typical branched tubuloalveolar formation of the Harderian gland with a small focal lymphocytic aggregate.
Section also includes portion of unremarkable optic nerve and extraocular muscles.
(58957)

Brain

Sections were prepared from the standard levels of the brain:

Level I forebrain: including cortex, corpus callosum, caudate putamen and lateral ventricles (Bregma 0.50mm)
Level II midbrain: including the hippocampus, thalamus, hypothalamus and lateral and third ventricles (Bregma -2.06mm)
Level III hindbrain: includes the cerebellum, pons and fourth ventricle (Bregma -5.80mm)

Sections of brain stained with Haematoxylin and Eosin, Luxol Fast Blue appear symmetrical with no ventricular dilation observed, unremarkable meninges and typical lamination.
The cerebellum appears symmetrical with typical architecture and Purkinje cells.
There was no evidence of neuronal loss and the myelination appeared normal.

(58969, 58970)
No lesions of significance

Comments:

Neuropatholoy to comment

Spinal cord

Representative thoracic and lumbar region of spinal cord, vertebral bone, intervertebral disc, striated muscle, peripheral nerves and bone marrow.
(58960)
No lesions of significance

Comments:

Neuropatholoy to comment

(Hind leg) Long bone/Bone marrow/Synovial joint/Skeletal muscle

Section shows unremarkable long bone, striated muscle, synovial joint and bone marrow including conspicuous megakaryoblasts. The skeletal muscle shows consistent fiber size with peripheral nuclei.
(58951)
No lesions of significance

Head

Multiple levels through the head demonstrate dermal appendages, nasal cavity, oral cavity, teeth and tongue including muscle bundles. Sections also show unremarkable pituitary gland including pars intermedia, pars distalis and pars nervosa as well and the trigeminal nerve/ganglia (58971). The outer and middle regions of the ear are discernible. The tympanic membrane is intact and the ossicles are unremarkable and include the stapedial annular ligaments (58972, 58973). Typical components of the inner ear including bony labyrinth, organ of corti, stria vascularis and scala cavities are discernible. Based on multiple levels, the organ of corti is unremarkable with no discernible loss of inner/outer hair cells and typical tectorial membrane (58972-58974).
The cochlear nerve and spiral ganglion is also demonstrated and based on several levels, there is no reduction in the density of the spiral ganglion cells. Examples of otolith organs can be seen with typical features such as the hair cells and mineral otoliths. The ampulla including the crista ridge with hair cells is discernible (58972, 58974).

No lesions of significance
(58971-58974)

ENU28 11 G7#360

Macro Observations

Spleen: 14x4x2mm
Kidneys: 10x6x5mm, symmetrical
Thymus: 8x7x2mm
Heart: 10x6x5mm
Brain: 14x9x5mm, symmetrical
Pituitary gland identified, macroscopically normal
Tail 78mm (straight)
Teeth, tongue and oral mucosa unremarkable - Head harvested for evaluation of auditory and vestibular structures
Tail suspension test for neurological defects-negative

Tissue presumed to be gall bladder - very dark brown/grey 3x2x2mm

Micro Observations

Marrow smear: Examination of the smear showed representative cells from the myeloid and erythroid series. Conspicuous cells from the lymphoid series. Numerous and unremarkable megakaryoblasts.
(58949)

Peripheral blood smear: Examination of the smear showed red blood cells (majority of cells shown), occasional white blood cells including lymphocytes, segmented neutrophils, platelets (clumps) and monocytes. No discernible morphological changes or detectable parasites.
(58948)

Mammary glands

Section shows typical mammary fat pad with developing lactiferous ducts, blood vessels and nerve bundles. Some scattered mast cells identified; a common finding in mouse mammary tissue.
(58928)
No lesions of significance

Ovaries/Oviducts

Section shows ovaries containing follicles at various stages of development (primary through to antral), several corpora lutea and mild interstitial age related ceroid-lipofuscin laden cells.
Unremarkable oviduct micromorphology with typical columnar epithelium and mucosal folds.
Query - portions of serosa appear mildy cystic.
(59374, 59375)

Comments:

Pathology to comment

Uterus/Cervix/Vagina/Clitoral gland

The architecture of the endometrium/endometrial glands, myometrium and adventitia are discernible.
Moderate cystic endometrial hyperplasia (58929, 59374, 59375), a common age related lesion, and mild focal lymphocytic perivascular infiltrates near the vagina (59375).
Some neutrophils and low numbers of lymphocytes identified in the endometrial glands; a common finding within a non-inflamed endometrium during the phases of estrus.
The micromorphology of the uterus and vagina places the animal at metestrus.
(58929, 59374, 59375)

Urinary Bladder

Collapsed bladder with typical urothelium and detrusor muscle.
Mild focal lymphocytic aggregate within the submucosa (59374).
Section includes unremarkable urethra.
(58929, 59374, 59375)

Liver/Gall bladder

Section shows liver parenchyma including hepatocytes, Kupffer cells, portal triads and central veins.
Mild multifocal periportal inflammatory aggregates (a common finding in the mouse) and mild focal perivascular lymphocytic infiltrates.
Unremarkable Gall bladder.
(58934)

Stomach

Section shows unremarkable fore and glandular portions of the stomach with limiting ridge.
Section also includes pylorus sphincter and duodenal bulb.
(58923)
No lesions of significance

Small Intestine (Duodenum, Jejunum & Ileum)/GALT

Section shows typical mucosal villi and submucosal layers.
Peyer’s patches displayed typical reactive nodal histology.
(58936, 58940)
No lesions of significance

Cecum/Colon/GALT

Typical mucosal folds and submucosal layers and occasional lymphoid cluster (Peyer's patch)
(58932, 58941)
No lesions of significance

Mesenteric lymph node

Section does not include mesenteric lymph node

Spleen

Unremarkable follicular pattern identified with typical red and white pulp micromorphology.
Moderate extramedullary hematopoiesis and Hemosiderin laden macrophages identified in the red pulp of the spleen, a common finding in the mouse.
(58924)
No lesions of significance

Pancreas

Section shows representative exocrine tissue (serous acini) and endocrine tissue (islets of Langerhans) with mild multifocal perivascular lymphocytic infiltrates.
(58924, 58940)

Kidney

Section shows a cortex, medulla, and papilla with uniform distribution of Glomeruli and accompanying nephron components.
Mild multifocal perivascular lymphocytic infiltrates, and a few protein casts within the medulla and papilla.
Section also includes renal lymph nodes with typical reactive nodal histology and mild sinus histiocytosis.
(58935, 59373)

Adrenal glands

Section shows adrenal glands with typical cortex/medulla distribution with a few age related lipofuscin laden cells at the cortical-medullary junction and mild subcapsular spindle cell hyperplasia, a common background lesion.
(58935, 59373)

Salivary glands and Regional lymph nodes

Mild multifocal perivascular lymphocytic infiltrates within the submandibular gland and unremarkable sublingual and parotid glands.
The regional lymph nodes displayed mild follicular hyperplasia with germinal centre formation, indicating a reactive state.
(58926)

Thyroids

Normal lateral lobes of the thyroid gland with typical colloid secreting follicles lined by cuboidal epithelium.
(58931)
No lesions of significance

Trachea/Lungs

Section shows lung micromorphology demonstrating parenchyma/alveoli, bronchioles, blood vessels and parabronchial lymph node with mild focal perivascular lymphocytic infiltrates.
Trachea with unremarkable mucosal epithelial lining and hyaline cartilage.
Oesophagus with typical features including stratified squamous epithelium.
(58931)

Thymus

Section shows typical medulla/cortex distribution and micromorphology.
(58930)
No lesions of significance

Heart/chambers/vessels/valves

Section shows cardiac muscle, chambers, valves and vessels of the heart.
The cardiac muscle fibres demonstrated typical features including central nuclei, branching fibres and striations.
Query: eosinophilic islands within the myocardium judged to be degenerating myocytes.
(58938)

Comments:

Pathology to comment

Skin

Typical dermal appendages and distribution. Unremarkable thin layer of striated muscle (panniculus carnosus).
(58927)
No lesions of significance

Tail

Section shows typical tail components including keratinized squamous epithelium, dense regular connective tissue, tendons, caudal vertebra, bone marrow, intervertebral disc, skeletal muscle, nerves and blood vessels.
(58922)
No lesions of significance

Eyes/Harderian glands

Section shows eyes with unremarkable retina, cornea, iris, ciliary body, lens, sclera and choroid.
Typical branched tubuloalveolar formation of the Harderian gland and a mild focal lymphocytic inflammtory infiltrates.
Section also includes portion of unremarkable optic nerve and extraocular muscles.
(58939)

Brain

Sections were prepared from the standard levels of the brain:

Level I forebrain: including cortex, corpus callosum, caudate putamen and lateral ventricles (Bregma 0.74mm)
Level II midbrain: including the hippocampus, thalamus, hypothalamus and lateral and third ventricles (Bregma -0.82mm)
Level III hindbrain: includes the cerebellum, pons and fourth ventricle (Bregma -5.80mm)

Sections of brain stained with Haematoxylin and Eosin, Luxol Fast Blue appear symmetrical with no ventricular dilation observed, unremarkable meninges and typical lamination.
The cerebellum appears symmetrical with typical architecture and Purkinje cells.
There was no evidence of neuronal loss and the myelination appeared normal.

(58933, 58942)
No lesions of significance

Comments:

Neuropatholoy to comment

Spinal cord

Representative thoracic and lumbar region of spinal cord, vertebral bone, striated muscle, peripheral nerves and bone marrow.
(58933)
No lesions of significance

Comments:

Neuropatholoy to comment

(Hind leg) Long bone/Bone marrow/Synovial joint/Skeletal muscle

Section shows unremarkable long bone, striated muscle, synovial joint and bone marrow including conspicuous megakaryoblasts. The skeletal muscle shows consistent fiber size with peripheral nuclei.
(58937)
No lesions of significance

Head

Multiple levels through the head demonstrate dermal appendages, nasal cavity, oral cavity, teeth and tongue including muscle bundles. Sections also show unremarkable pituitary gland including pars intermedia and pars distalis as well and the trigeminal nerve/ganglia (58943).
The outer and middle regions of the ear are discernible. The tympanic membrane is intact and the ossicles are unremarkable and include the stapedial annular ligaments (58944, 58945).
Stria vascularis of the inner ear is discernible (58944, 58945).
Examples of otolith organs can be seen with typical features such as the hair cells and mineral otoliths. The ampulla including the crista ridge with hair cells is discernible (58944, 58945).

No lesions of significance
(58943, 58945)

Comment / Plan

Case APN16/042 will be referred to Professor Rolfe Howlett R&A Pathology Services NSW and Professor Catriona McLean, Anatomical Pathology, Alfred Hospital Melbourne for comment.

Aira Nuguid
1st February, 2017

Revised by AN
8th February, 2017

Supplementary Pathology Report

ENU28 11 G7#338 (control)

ENU28 11 G7#340 (control)

ENU28 11 G7#345 (control)

ENU28 11 G7#355

Ovary/ Fallopian tubes/Uterus / Vagina

The ovaries contain varying stages of follicles, several corpora lutea and mild to moderate ceroid –lipofuscin laden cells. Unremarkable oviduct micromorphology. No other changes of significance.
Mild cystic hyperplasia of the uterus. The uterus and vagina display features that place the mouse in metoestrus. The lining of the stratified squamous epithelium has lost the keratinisation layer and inflammatory cells occur along the lumenal surface of the vaginal wall.

Urinary Bladder

The bladder wall is distended with the urothelium easily discernible. No lesions of significance. There is no inflammatory change of significance

Liver /Gall Bladder

A solitary island of mixed mononuclear inflammatory cells that involved two hepatic acini. However as this is solitary and not active, the inflammatory lesion is not significant.

Oesophagus

The sections from the mediastinal region does not reveal any lesion of significance.

Kidneys

Sections contain both kidneys displaying cortex , medullary rays, medulla and the pelvis. Even spread of glomeruli through the renal parenchyma. Protein casts were occasionally observed some appeared to extend into the terminating microcysts particularly in the medulla. Accumulation of mainly lymphocytes was around the peripelvic tissue. The accumulation of mononuclear inflammatory cells peri-pelvically often seems to occur as the mice age.
No lesions of significance

Adrenal glands

No lesions of significance with a few ceroid-lipofuscin containing cells at the cortico-medullary junction

Thyroid glands

Lateral lobe of the thyroid with colloid secreting follicles lined by cuboidal epithelium
No lesions of significance

Salivary glands and associated Lymph nodes

A mild focal area of perivascular/periductal chronic inflammation. Cells were mononuclear and mainly lymphocytes; the inflammation is not active.

The lymph nodes display a mild follicular hyperplasia and mild sinus histiocytosis.
These features within the node are within the range of an expected reactive state of the nodes.

Lungs/ Trachea /Bronchi

A large island of small mainly reactive lymphocytes occurs in a parabronchial location;
this might represent part of the parabronchial lymph node particularly as this area has several readily distinguished small blood vessels as though this area has an established vascular supply vascular . This lymphocytic dominated area does not represent an active focus of inflammation.
Minimal significance especially as the mouse is older than 1 year.

Heart / major vessels / valves

Sections reveal normal right and left ventricles. The aortic valves and the atria-ventricular valves were present. The valves had varying degrees of valvular myxomatous thickening in different sites/locations
As many strains of mice age this is not an uncommon finding. If the thickening is at the valvular edge then this can and does lead to a cardiac incompetence.

ENU28 11 G7#359

Ovary/ Fallopian tubes/Uterus

Sections reveal follicles at different development stages , several corpora Lutea and interstitially there were macrophages filled with ceroid-lipofuscin.
Unremarkable oviducts (Fallopian tubes) although the lining epithelium is patchily vacuolated
Moderate cystic endometrial hyperplasia of the uterus.(These changes seem age related to a major extent).
The micromorphology of the uterine wall particularly the inflammatory cells(neutrophils and lymphocytes) suggests that this female mouse is probably in one of the phases of oestrus.

Urinary Bladder

The features of the urinary bladder wall and the urethra had no lesions of significance

Liver /Gall Bladder

Sections display features of liver and its gall bladder. The microscopic pathology seemed to be without lesions of significance. However, there were scatterings and large nests (over the size of an acinus) of mononuclear inflammatory cells (mainly lymphocytes with a few macrophages) through the hepatic parenchyma.
These changes observed are no longer active or of significance. However the multiplicity of the inflammatory cellular clusters are indicative of previous inflammatory responses either singly (additional) or multiple at a single time point.

Oesophagus

Mediastinal sections display normal oesophagus in the thorax.

Kidneys

Sections display a normal microscopic pattern of the cortex, medulla and pelvis.
The renal parenchyma had less that 5 mononuclear inflammatory cellular nests of varying size some were located peri-pelvically while others near to the cortico-medullary junction.
These cellular aggregates did not display features of activity and were judged not to be of significance.
Proteinaceous casts were occasionally observed.

Adrenal glands

The adrenal gland showed subcapsular spindle cell hyperplasia that had expanded vertically and horizontally. This feature has been attributed to hormonal alteration and is observed more frequently with aging mice.(ref: "Pathology of the Mouse" edited by Robert R Maronpot.

Thyroid glands

No lesions of significance in the lateral lobe of the thyroid gland. A small parathyroid gland nestled in the thyroid tissue.

Salivary glands and associated Lymph nodes

Present in the sections were parotid, sublingual and submandibular salivary glands.
In one large lobe of the parotid gland there was a diffuse acute on chronic sialadenitis with an early regeneration. The most likely cause would be bacteria.

Additionally, there was a basophilic hypertrophic focus consisting of a foci of enlarged acinar glands. Such lesions have only been encountered in the parotid gland.

The regional lymph nodes displayed features consistent with a status of immuno-reactivity.

Lungs/ Trachea /Bronchi

The left lung is without any lesion of significance. However in the right lung there were multiple small nodules of mononuclear inflammatory cells most scattered in the stroma tissue of this lung.
The regional para-tracheal lymph node displays minor changes but on balance of little significance at the moment.
Microscopic foci and individual alveolar macrophages contain within their cytoplasm eosinophilic bodies/crystals.

Thymus

Medulla and cortex distribution as described within the thymus.
There is a thymic cyst which appeared as thought it may have arisen from epithelial hyperplastic elements.
Cysts are a common finding in the involuted thymus of aged mice. Thymic cysts were reported in control mice up to four to five percent. "Pathology of the mouse" edited by Robert R Maronpot.

Heart / major vessels / valves

Sections reveal normal right and left ventricles. The aortic valves and the atria-ventricular valves were present. The valves had varying degrees of valvular myxomatous thickening in different sites/locations
As many strains of mice age this is not an uncommon finding. If the thickening is at the valvular edge then this can and does lead to a cardiac incompetence.

ENU28 11 G7#360

Ovary/ Fallopian tubes & Uterus / Vagina

Both ovaries were sectioned and revealed follicles, corpora lutea and some interstitial cells containing ceroid-lipofuscin. Serosa appeared irregular in areas and possibly cystic probably nothing more than fixation artefact. The oviducts were lined by folded epithelial lining. Some of lining epithelial cells were vacuolated.

Moderate cystic endometrial hyperplasia has disturbed somewhat the microanatomy of these tissues.
The micromorphology of the epithelium particularly of the vagina displays that the stratified squamous epithelium is being thinned actively by clusters of mainly mononuclear inflammatory cells. Such a pattern is consistent with the animal being in the oestrus cycle e.g. phase metoestrus

Urinary Bladder

Normal epithelial lining and detrusor muscle

Heart

sections reveal a left and right ventricle and portions of the left and right atria.
A portion of the atria ventricular valve and one aortic valve have a noticeable thickening. Hence depending upon where the thickening is will determine whether the lesion has an effect of the cardiac output.

Summary

Please refer to above comments

Professor Rolfe Howlett
R&A Pathology Services, NSW
16th February, 2017

Supplementary Neuropathology Report

ENU28 11 G7#338 (control)

H&E and LFB stained brain sections were examined.
Representative H&E stained sections of spinal cord were examined.
Slides were used as histological controls.

ENU28 11 G7#340 (control)

H&E and LFB stained brain sections were examined.
Representative H&E stained sections of spinal cord were examined.
Slides were used as histological controls.

ENU28 11 G7#345 (control)

H&E and LFB stained brain sections were examined.
Representative H&E stained sections of spinal cord were examined.
Slides were used as histological controls.

ENU28 11 G7#355

H&E and LFB stained brain sections were examined.
Representative H&E stained sections of spinal cord were examined.
Sections of brain and spinal cord show no significant neuropathology.

ENU28 11 G7#359

H&E and LFB stained brain sections were examined.
Representative H&E stained sections of spinal cord were examined.
Sections of brain and spinal cord show no significant neuropathology.

ENU28 11 G7#360

H&E and LFB stained brain sections were examined.
Representative H&E stained sections of spinal cord were examined.
Sections of brain and spinal cord show no significant neuropathology.

Summary

Sections of brain and spinal cord show no significant neuropathology.

Professor Catriona A McLean
BSc, MBBS, FRCPA, MD, FFSc (RCPA)
Head, Dept of Anatomical Pathology, Alfred Health
Professor, Central Clinical School, Monash University
Professor, The Florey Institute of Neuroscience and Mental Health
Head, Victorian Neuromuscular Laboratory Services, Alfred Health
Director, Victorian Brain Bank at The Florey
3rd February, 2017

The Australian Phenomics Network advises all research groups that images or results obtained through the services offered by the APN are to be acknowledged in resultant publications. Example acknowledgement: "This study utilised the Australian Phenomics Network Histopathology and Organ Pathology Service, University of Melbourne."

Authorised by Tina Cardamone, APN Histopathology and Organ Pathology Node manager.